Nucleic Acids Research, 2025, gkaf1521
https://doi.org/10.1093/nar/gkaf1521
Standard Article

NSMF modulates replication stress to facilitate colorectal cancer progression

Kyeong Jin Shin [1,†], Yu Jin Lee [1,2,†], Gyuri Kim [1], Seongjun You [1], Kyoung Lock Kim [3,4], Sabin Park [5], KyoungJun Lee [5], Eun A Lee [6], Do Hong Park [1], Hui Won Kim [1], Sanga Choi [7], Sung Min Jung [8], Jung-Hyun Kim [7], Jang Hyun Choi [1], Hyung-Sik Kim [9], Kyungjae Myung [5,6], Semin Lee [5], Seung-Jae Myung [10], Young Chan Chae [1,*]

[1]Department of Biological Sciences, Ulsan National Institute of Science and Technology, Ulsan 44919, Republic of Korea
[2]National Creative Research Center for Cell Plasticity, KAIST Stem Cell Center, Department of Biological Sciences, KAIST, Daejeon 34141, Republic of Korea
[3]Department of Pathology, Dana-Farber Cancer Institute, Boston, MA 02215, United States
[4]Broad Institute of MIT and Harvard, Cambridge, MA 02142, United States
[5]Department of Biomedical Engineering, College of Information-Bio Convergence Engineering, UNIST, Ulsan 44919, Republic of Korea
[6]Center for Genomic Integrity, Institute for Basic Science, Ulsan 44919, Republic of Korea
[7]Research Institute, National Cancer Center, Goyang10408,Republic of Korea
[8]Department of Surgery, Inje University, Ilsan Paik Hospital, Goyang10380, Republic of Korea
[9]Department of Oral Biochemistry, Dental and Life Science Institute, School of Dentistry, Pusan National University, Yangsan 50612, Republic of Korea
[10]Department of Gastroenterology, University of Ulsan College of Medicine, Asan Medical Center, Seoul 05505, Republic of Korea

*To whom correspondence should be addressed. Email: ychae@unist.ac.kr
†The first two authors should be regarded as Joint First Authors.

Abstract

Cancer cells precisely modulate replication stress to sustain genomic instability without triggering lethal DNA damage, yet regulators enabling this delicate balance remain largely unknown. Here, we identify N-methyl-D-aspartate receptor synaptonuclear signaling and neuronal migration factor (NSMF) as a novel and critical regulator of replication stress in colorectal cancer (CRC). NSMF expression is significantly elevated in CRC tissues and correlates closely with elevated replication stress. In *Apc*$^{Min/+}$ mouse models, *Nsmf* knockout selectively induces replication-dependent DNA damage in tumor tissues, suppressing tumor growth and prolonging survival, without harming normal tissues. Mechanistically, NSMF deficiency impairs replication fork progression under stress conditions, resulting in DNA damage accumulation, growth arrest, and senescence. Conversely, NSMF overexpression provides resistance to oncogene-induced replication stress, enabling cancer cells to evade senescence and sustain proliferation. These findings establish NSMF as an essential safeguard against lethal replication stress and highlight its potential as a promising therapeutic target for CRC treatment.

Graphical abstract

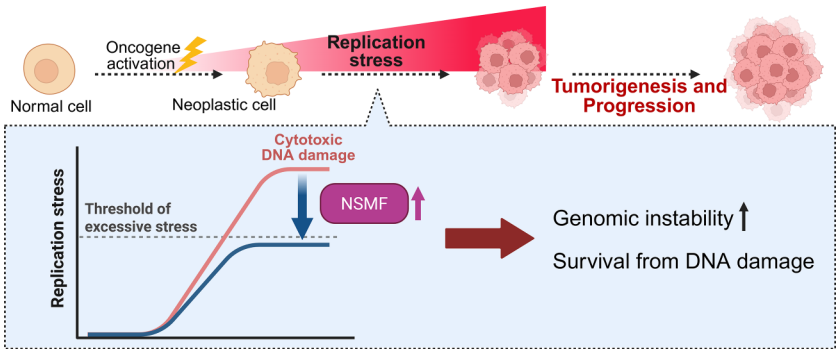

Introduction

Accurate and complete DNA replication is essential for cellular proliferation and genome stability. To ensure fidelity, DNA replication is a highly regulated and complex process involving the coordinated activity of hundreds of proteins. However, disruptions in this process, collectively known as replication stress, can lead to slowed, stalled, or collapsed

Received: August 12, 2025. **Revised:** November 30, 2025. **Accepted:** December 20, 2025

replication forks, thereby compromising genome integrity [1]. Multiple factors contribute to replication stress, including nucleotide depletion, transcription–replication conflicts, difficult-to-replicate genomic regions, and aberrant firing of replication origins [2–6]. Cells typically mitigate replication stress by activating DNA damage response (DDR) pathways, specialized networks of proteins that detect and resolve replication obstacles to restore fork progression [7, 8]. When these protective mechanisms are overwhelmed or impaired, unresolved replication stress leads to both focal and large-scale genetic alterations—such as point mutations, chromosomal rearrangements, and aneuploidy—which are hallmarks of genomic instability that drive cancer initiation and progression [9–13].

Cancer cells inherently experience elevated replication stress due to genetic alterations disrupting DNA replication and repair balance. In colorectal cancer (CRC), mutations in key oncogenes and tumor suppressors, such as APC, KRAS, MYC, and PIK3CA, drive tumor progression by promoting uncontrolled proliferation, thereby increasing replication stress. Concurrent mutations in DDR genes, such as TP53, BRCA1/2, ATM, ATR, and mismatch repair (MMR) components, further impair the cell's ability to alleviate replication stress, reinforcing genomic instability. Consequently, CRC exemplifies a cancer type where chronic replication stress significantly influences tumor initiation and progression [14–16]. However, replication stress functions as a double-edged sword in cancer. While moderate levels promote tumor evolution and malignant progression, excessive stress induces detrimental DNA damage, proliferation arrest, and cell death. Indeed, early tumorigenic events such as oncogene activation or tumor suppressor loss initially trigger severe replication stress, provoking apoptosis or senescence as intrinsic protective mechanisms that limit tumor growth [17–19]. To sustain growth and survival, cancer cells must precisely calibrate replication stress—leveraging its oncogenic advantages while preventing excessive damage that compromises viability. Given the essential role of replication stress balance in cancer cell survival, therapeutic strategies that either exacerbate replication stress or interfere with stress tolerance mechanisms have shown potential to selectively eliminate tumor cells [2, 20]. Conventional chemotherapeutic agents, such as nucleoside analogs (e.g. gemcitabine) and DNA-damaging agents (e.g. cisplatin), increase replication stress beyond tolerable thresholds; however, their clinical utility is often limited by low selectivity and significant systemic toxicities [2]. To overcome these limitations, recent therapeutic development has focused on targeting cancer-specific regulators of replication stress tolerance, notably DDR kinases such as ATR, CHK1, and WEE [21–26]. Nonetheless, these kinase inhibitors face ongoing challenges, including therapeutic resistance and dose-limiting toxicities in normal tissues [24]. Thus, identifying tumor-specific regulators that precisely modulate the replication stress response is crucial for understanding how cancer cells adapt to replication-associated challenges and for developing precision therapies that exploit these vulnerabilities.

In this study, we investigated factors critical for managing replication stress, essential for cancer cell survival and proliferation. N-methyl-D-aspartate receptor synaptonuclear signaling and neuronal migration factor (NSMF), originally characterized in neuronal development and Kallmann syndrome, has recently been implicated in the DDR [27–29]. We demonstrated that NSMF physically interacts with replication protein A2 (RPA2), facilitating its recruitment to single-stranded DNA (ssDNA) and stabilizing the RPA–ssDNA complex, which is essential for protecting exposed DNA strands and recruiting DDR proteins [30, 31]. Loss of NSMF disrupts ATR signaling and DNA repair increasing sensitivity to replication stress-inducing agents such as hydroxyurea and ionizing radiation [30]. Despite these insights, NSMF's specific functional role in cancer has remained largely unexplored.

Here, we extend the established biochemical role of NSMF into the pathological context of CRC. We demonstrate that NSMF fine-tunes replication stress in the setting of oncogenic pressure, preventing catastrophic DNA damage while allowing the level of genomic instability that fuels CRC development. Through integrated analyses of CRC patient specimens, cellular models, and CRC mouse model, we identify NSMF as a cancer-specific dependency and a potential therapeutic vulnerability. These findings suggest that targeting NSMF may offer a selective strategy to impair CRC cell survival without compromising normal tissue integrity.

Materials and methods

Cell culture

The normal colon-derived cell line CCD-18Co, human CRC cell lines HCT116, and the human lung fibroblast cell line IMR-90 were obtained from the American Type Culture Collection (ATCC, Manassas, VA). Human CRC cell lines LS513, SNU-407, RKO, DLD-1, SW620, and SW480 were acquired from the Korean Cell Line Bank (KCLB, Korea). All cell lines were maintained under the recommended culture conditions specified by the respective suppliers. All commercial cell lines were authenticated by the suppliers and routinely tested for Mycoplasma contamination in the laboratory.

Antibodies and reagents

The following primary antibodies were used for western blot Antibodies against NSMF (Aviva System Biology, Cat# OAAN03468), γH2AX (Cell Signaling Technology, Cat# 9718), β-Actin (GeneTex, Cat# GTX629630), GAPDH (Santa Cruz, Cat# sc-32233), α-Tubulin (GeneTex, Cat# GTX112141), H2B (Millipore, Cat# 07-371), pT1989-ATR (Cell Signaling Technology, Cat# 30632), ATR (Santa Cruz, Cat# sc-515173), pS345-CHK1 (Cell Signaling Technology, Cat# 2348), pS317-CHK1 (Cell Signaling Technology, Cat# 2344), CHK1 (Santa Cruz, Cat# sc-8408), pS33-RPA2 (Bethyl Laboratories Inc., Cat# A300-246A), RPA2 (Bethyl Laboratories Inc., Cat# A300-244A), p16^INK4A (Cell Signaling Technology, Cat# 80 772), p21 Waf1/Cip1 (Cell Signaling Technology, Cat# 2947), Ras (Cell Signaling Technology, Cat# 14412), Cyclin D1 (Cell Signaling Technology, Cat# 2978), PARP (Cell Signaling Technology, Cat# 9532), Cleaved PARP (Cell Signaling Technology, Cat# 9541), Caspase 3 (Cell Signaling Technology, Cat# 9662), and Cleaved Caspase 3 (Cell Signaling Technology, Cat# 9661). Antibodies against Ki-67 (Abcam, Cat# 16667), Cleaved Caspase 3 (Cell Signaling Technology, Cat# 9661), and γH2AX (Cell Signaling Technology, Cat# 9718) were used for immunohistochemical staining. Antibodies against pS33-RPA2 (Bethyl Laboratories Inc., Cat# A300-246A) and γH2AX (Sigma–Aldrich, Cat# 05-636) were used for immunofluorescence analysis.

RNAi-based knockdown and ectopic expression experiments

For lentiviral-mediated NSMF knockdown, specific lentiviral expression vectors targeting human NSMF (NSMF#1: Sigma–Aldrich, TRCN0000165475; NSMF#2: Sigma–Aldrich, TRCN000016551) or a non-silencing control plasmid (pLKO.1-puro, Sigma–Aldrich, Cat# SHC002) were used. Recombinant and control lentiviruses were produced by co-transfecting 293T cells with VSVG and delta 8.9 packaging plasmids using Lipofectamine 2000 Reagent (Invitrogen, 11668019). Lentiviral particles were harvested from the conditioned medium at 24 and 48 h post-transfection, followed by centrifugation to remove cells and debris and filtration through a 0.45-μm filter. HCT116 cells (2×10^5 per well in six-well plates) were transduced with 0.5 ml of viral suspension containing 4 μg/ml Polybrene (Sigma–Aldrich) for 24 h. Puromycin-resistant clones (2 μg/ml) were selected using the limiting dilution method. The efficiency of *NSMF* knockdown was validated by quantitative polymerase chain reaction (PCR) and western blot analysis.

For siRNA-mediated NSMF knockdown, cancer cell lines were transfected with either non-targeting siRNA (Bioneer, Korea, #SN-1002) or *NSMF*-targeting siRNAs (NSMF#1: CTCAGACGTTGCTCAGGTT; NSMF#2: CAGATGATCGAGACGTACT). HCT116 cells were seeded at 2×10^5 cells per well in six-well plates and incubated for 24 h before transfection. The *NSMF*-specific siRNA was diluted to a final concentration of 10 nM in 100 μl OptiMEM (Gibco), mixed with 2 μl Lipofectamine RNAiMAX (Invitrogen, 13778150) prediluted in 100 μl OptiMEM. After washing with 1 ml OptiMEM, cells were incubated with the siRNA-containing mixture for 6 h, followed by an additional 42-h culture in fresh medium. A scrambled non-silencing siRNA duplex (siCTRL) was used as a control. Knockdown efficiency was assessed 48 h post-transfection.

The H-Ras^{G12V} viral vector was obtained from Addgene (#22262). To generate the GFP-tagged NSMF viral vector, an N-terminal GFP fusion was inserted into the NSMF open reading frame and cloned into the pReceiver-Lv105 lentiviral vector (Genecopoeia). For oncogene-induced senescence, IMR-90 cells were seeded at 5×10^5 cells per 100-mm dish and incubated for 24 h before transduction with lentiviruses encoding GFP-NSMF or GFP-vector, as described above. After 24 h, the medium was replaced with fresh G418-containing medium (200 μg/ml) and maintained for 3 days. The cells were then infected with either control or Ras^{G12V} lentivirus for 24 h, followed by selection in puromycin-containing medium (2 μg/ml) for 2 days.

Proliferation assay

Cell proliferation was assessed by directly measuring changes in cell number over time. For cell counting assays, triplicate aliquots of 1×10^4 cells from each clone and a control cell line were seeded on 12-well plates. At 24-h intervals, cells were harvested by trypsinization, counted on a cell counter (Invitrogen), and normalized to the initial (day 0) cell counts.

Colony formation assays

Cells were plated at a density of 1×10^3 cells per well in 12-well culture plate in triplicate and allowed to adhere for 24 h before treatments. For drug treatment, small-molecule inhibitors (Olaparib, VE-821, and Rabusertib) were used at concentrations ranging from 0.5 to 4 μM for 72 h, with equivalent volumes of the vehicle (DMSO, ≤0.1%) used as controls. After 3 days of drug treatment, the medium was replaced with fresh inhibitor-free medium, and cells were allowed to growth for an additional 3 days before analysis. For siRNA experiments, cells were transfected with NSMF or control siRNA using Lipofectamine RNAiMAX (Invitrogen) according to the manufacture's protocol. After transfection, cells were incubated for 6 days before further analysis. Colonies were washed with 1× phosphate buffered saline (PBS), fixed with formalin, and stained with 0.5% (w/v) crystal violet solution. Plates were rinsed with tap water, and images were captured using a digital scanner. n. Image analysis was performed using ImageJ software (v1.54f), and EC50 values were calculated using GraphPad Prisim (Version 8).

SA- β- galactosidase staining

Senescence-associated β-galactosidase (SA-β-gal) staining was performed using the Senescence β-Galactosidase Staining Kit (Cell Signaling Technology #9860) following the manufacturer's instructions. Briefly, growth media were removed, and the cells were rinsed once with 1× PBS (2 ml for a six-well plate). Cells were then fixed with 1 ml of 1× Fixative Solution for 10–15 min at room temperature. After fixation, the cells were rinsed twice with 1× PBS. At this point, plates could either be used immediately for staining or stored in 1× PBS at 4°C overnight, covered. Next, 1 ml of β-Galactosidase Staining Solution was added to each well, ensuring proper preparation as per the kit protocol. Plates were sealed with parafilm to prevent evaporation, which could lead to crystal formation, and incubated at 37°C in a dry, CO_2-free incubator overnight to allow color development. The absence of CO_2 was critical to maintain the solution's pH and ensure reliable staining. After incubation, cells were examined under a microscope at 200× magnification for blue staining, indicative of senescence. For long-term storage, the staining solution was removed, and the cells were overlaid with 70% glycerol and stored at 4°C. The percentage of senescent cells was calculated by quantifying blue-stained cells relative to the total cell count.

Flow cytometry

Cells were counted, plated, and allowed to adhere overnight. The next day, bromodeoxyuridine (BrdU) was added to the medium for 1 h, after which the cells were collected and fixed according to manufacturer's protocol (BD Biosciences, #552598). Samples were analyzed in duplicate using a NovoCyte flow cytometer (Agilent), and data were processed with FlowJo software (BD Biosciences) to determine G1, S, and G2/M populations.

Annexin V staining was performed using the FITC Annexin V Apoptosis Detection Kit (Invitrogen, #BMS500FI) according to the manufacturer's instructions. After the indicated treatment, cells were washed twice with ice-cold PBS and resuspended at 1×10^6 cells per ml in 1× binding buffer provided in the kit. The 100 μl of cell suspension (containing 1×10^5 cells) were transferred to a 5 ml round-bottom tube. Then, 5 μl of FITC Annexin V and 5 μl of PI staining solution were added to each tube, followed by gently vortexing and incubation for 15 min at room temperature in the dark. Finally, 400 μl of 1× binding buffer was added to each tube. Stained cells were analyzed using the NovoCyte flow cytometer (Agilent).

DNA fiber assay

DNA combing analysis was performed as previously described [32], with minor modifications. Briefly, cells were pulse-labeled with 100 μM CldU (5-chloro-2′-deoxyuridine, Sigma–Aldrich, C6891) for 30 min, followed by 250 μM IdU (5-iodo-2′-deoxyuridine, Sigma–Aldrich, I7125) for 30 min, with or without hydroxyurea (HU; 2 mM, Sigma–Aldrich, H8627) treatment. Cell were collected by trypsinization and embedded into low-melting agarose (Bio-Rad 161-3112), followed by DNA extraction. To stretch the DNA fibers, 22 mm × 22 mm silanized coverslips (Genomic Vision) were dipped into the DNA solution for 13 min and pulled out a constant speed (300 μm/s). Coverslips were baked for 4 h at 60°C and incubated with acid for denaturation. CldU- and IdU-labeled DNA tracts were detected by rat anti-BrdU antibody (1:50–1:100, detects BrdU and CldU; Abcam, 6326) and mouse anti-BrdU antibody (1:10–1:50, detects BrdU and IdU; Becton Dickinson 347580) for 2 h at room temperature. Coverslips were fixed in 4% paraformaldehyde/PBS and incubated for 1 h at room temperature with Alexa Fluor 488-conjuagated goat anti-rat antibody (1:100, A21208; Molecular Probes/Thermo Fisher) or Alexa Fluor 568-conjugated goat anti-mouse antibody (dilution 1:100, A21124; Molecular Probes/Thermo Fisher). Finally, coverslips were mounted with ProLong® Gold Antifade Reagent (Molecular Probes) and stored at −20°C. Images were acquired with an Axio Observer 7 (Carl Zeiss) and ApoTome2 (63× objective lens), and at least 200 DNA fibers were analyzed per experiment. Image acquisition and analysis were performed using ImageJ software program.

RNA extraction and qRT-PCR analysis

Total RNA was extracted using TRIzol reagent (Invitrogen) to evaluate expression of NSMF and senescence-associated secretory phenotype (SASP)-related genes. Complementary DNA (cDNA) was synthesized using the cDNA Reverse Transcription Kit (Applied Biosystems, #4368814), and quantitative PCR (qPCR) was performed using the SYBR® Green I Master mix (Roche) on the LightCycler 480 (Roche) instrument. The primer sequences used for qPCR are listed in Supplementary Table S1. All experiments were performed in biological and technical triplicates. Relative fold differences in expression levels were determined using the △Ct method, and all reactions were normalized to β-actin as a reference gene.

Mouse models

All animal care and experiments were conducted in strict accordance with the Guide for the Care and Use of Laboratory Animals from the In Vivo Research Center at UNIST. All procedures involving animals were approved by the Institutional Animal Care and Use Committee (IACUC) at Ulsan National Institute of Science and Technology (UNIST) (Protocol No. UNISTIACUC-22-24). All mice used in this study were of the C57BL/6 background and were housed in colony cages under specific pathogen-free conditions. Environment parameters were maintained at a temperature of 21–23°C, relative humidity of 50%–60%, and a 12-h light/12-h dark cycle. Only male mice were used in experiments, and food and water were provided ad libitum.

To generate CRC model, NSMF knockout (KO) mice (C57BL/6N-*Nsmf*$^{tm1a(KOMP)Wtsi}$) were crossed with *Apc*$^{min/+}$ mice, which were purchased from The Jackson Laboratory. *Nsmf*$^{+/-}$;*Apc*$^{min/+}$ were then intercrossed to generate *Nsmf*$^{+/+}$; *Apc*$^{Min/+}$ and *Nsmf*$^{-/-}$; *Apc*$^{Min/+}$mice. Genotyping was performed using the following primer sequences: *Nsmf*-A: 5′-GGC CCT GAG GTT ATT GAT GC-3′; *Nsmf*-B: 5′-GCT TGG CTT GAG GTG GTC TC-3′; *Nsmf*-C: 5′-TCG TGG TAT CGT TAT GCG CC-3′; *Apc* WT: 5′-GCC ATC CCT TCA CGT TAG-3′; *Apc* Min: 5′-TTC TGA GAA AGA CAG AAG TTA-3′; *Apc*-common: 5-TTC CAC TTT GGC ATA AGG C-3′. Mouse survival was continuously monitored for 60 weeks, and Kaplan–Meier survival curves were generated to assess overall survival. Mice were sacrificed at 16 and 20 weeks of age for transcriptome analysis and examine tumor formation assessment in intestine, respectively.

Primary MEF preparation and replicative senescence

Primary mouse embryonic fibroblasts (MEFs) were prepared according to the standard protocol [30]. Briefly, MEFs isolated from NSMF WT and KO mouse embryos at embryonic day 14.5 (E14.5) and plated at a density sufficient to achieve ∼50% confluence, which was designated as passage 0 (P0). Cells were subsequently passaged every 3 days. MEFs exhibited active proliferation for up to four passages but ceased division at late passages. Senescence markers and SASP factors were measured at passage 6.

Histology and immunohistochemistry

Tissues were fixed in 4% paraformaldehyde (PFA), dehydrated in ethanol, and embedded in paraffin. Sections were subjected to hematoxylin and eosin (H&E) and immunohistochemical (IHC) staining. For horseradish peroxidase (HRP)-DAB staining, 4-μm-thick formalin-fixed paraffin-embedded mouse tumors sections were deparaffinized, rehydrated and subjected to antigen retrieval using 10 mM sodium citrate buffer (pH 6.0). After blocking, sections were incubated with primary antibody overnight at 4°C. Immunostaining was performed using a rabbit-specific horseradish peroxidase/diaminobenzidine (HRP-DAB) detection IHC kit (Abcam, Ab64261) according to the manufacturer's instructions. After staining, sections were washed in running tap water, lightly counterstained with hematoxylin, dehydrated, and mounted using Micromount (Leica, 3801731). Sections were imaged with dotSlide (Olympus), image acquisition and analysis were performed using QuPath software (version.0.5.1).

Human tissue specimens and ethics statement

Histologically confirmed from CRC tissue adjacent non-tumor tissue was collected with informed patient consent, as approved by the Institutional Review Board of Asan Medical Center (IRB No. 2020-0969). Colonic mucosa and primary CRC tissue specimens were obtained during surgical resection at Asan Medical Center, Seoul, Korea. The use of patient tissues for research purposes was authorized by the local ethics committee of Asan Medical Center. All analyses were conducted anonymously, and written informed consent was obtained from all donors.

Immunofluorescence

Cells were grown on coverslips and harvested at 60%–70% confluency for immunofluorescent staining and GFP-tagging protein detection. For chromatin-bound RPA detection, cells

were first extracted with CSK buffer with 0.1% (vol/vol) Triton X-100 for 3 min on ice, washed with CSK buffer lacking Triton X-100, and fixed with 4% PFA for 20 min. Cells then blocked with 5% BSA, 0.25% Triton X-100 in PBS. For γH2AX detection, cells were fixed in 4% PFA in PBS for 10 min at RT, washed with PBS, and permeabilized with 0.25% Triton X-100 in PBS. Cells were blocked for 1 h in blocking buffer (3% BSA, 0.1% Tween-20 in PBS) and incubated with primary antibodies overnight at 4°C. After washing with 1× PBS, cells were incubated with fluorescent-conjugated secondary antibodies (Alexa Fluor 488 or 594, Thermo Fisher Scientific) for 1 h at RT. The slides were washed and mounted using Prolong Gold Anti-Fade mounting medium (Thermo Fisher Scientific). Nuclei were counterstained with DAPI. Images were acquired using a LSM 980N confocal microscope (Carl Zeiss) with 63× oil objective (1.46 NA) and analyzed using ImageJ software.

Western blot analysis

Protein samples were extracted using radioimmunoprecipitation assay buffer (RIPA buffer, Thermo Fisher Scientific) supplemented with a protease and phosphatase inhibitors cocktail (Thermo Fisher Scientific). Protein concentrations were measured using the bicinchoninic acid assay (Thermo Fisher Scientific). Samples were denatured by heating at 95°C for 5 min, after which the equal amounts of protein were loaded onto 10% sodium dodecyl sulfate (SDS)-polyacrylamide gel electrophoresis for electrophoresis and subsequently transferred to PVDF membrane (Millipore) for blotting. Membranes were blocked with 5% skim milk in Tris-buffered saline containing 0.1% Tween 20 (TBS-T) for 30 min at room temperature. Membranes were incubated with primary antibodies diluted in TBS-T overnight at 4°C, followed by incubation with HRP-conjugated anti-rabbit or anti-mouse secondary antibodies (1:5000 dilution; Seracare) for 1 h at room temperature. Immunoreactive bands were detected using an enhanced chemiluminescent (ECL) detection reagent (Cytiva, RPN2106) and visualized with the ChemiDoc imaging system (Bio-Rad). Band intensities were quantified using ImageJ software.

Chromatin fractionation analysis

Collected cells were washed in cold PBS and resuspended in NETN buffer at 4°C for 30 min. Crude cell lysates were centrifuged at 13 000 rpm at 4°C for 10 min, and the pellet was resuspended in 0.2 N HCl. Samples were incubated with rocking at 4°C for 1 h, and followed by centrifugation at 13 000 rpm at 4°C for 10 min. The chromatin-containing fraction was neutralized with 1 M Tris–HCl (pH 8.0) and prepared for western blotting. The chromatin fraction was boiled with 2× SDS sample buffer at 95°C for 10 min. Histone 2B (H2B) served as a control for the chromatic fraction.

Murine intestinal organoid culture

As previously reported [33] and briefly summarized here, small intestines were harvested, washed with cold PBS, opened laterally, and cut into 3- to 5-mm fragments. The tissue pieces were washed multiple times with cold PBS until no visible debris remained. To isolate epithelial crypt structures, the fragments were incubated with Gentle Cell Dissociation Reagent (STEMCELL Technologies) following the manufacturer's protocol. The resulting crypt suspensions were counted and embedded in growth factor-reduced Matrigel (Corning, #356231). Organoids were maintained in IntestiCult Mouse Organoid Growth Medium (STEMCELL Technologies, #06005) under standard culture conditions. The complete protocol is available at www.stemcell.com/technical-resources/area-of-inteerest/organoid-research.html.

Bulk RNA sequencing and analysis

Total RNA was extracted from mouse normal colonic tissue or adenomas using Trizol Reagent (Invitrogen, Carlsbad, CA), following the manufacturer's guidelines. RNA quantity was measured using the Qubit HS RNA assay (Thermo Fisher Scientific), and RNA integrity was assessed using the Fragment Analyzer HS NGS assay (AATI). Library preparation was performed using the MGIEasy RNA Directional Library Prep Kit (MGI, Shenzhen, China), and paired-end sequencing (150 bp) was conducted on a DNBSEQ-T7 platform, following the manufacturer's protocol. For RNA sequencing data processing, adapter sequences were removed using Cutadapt(v2.9), reads were quality-filtered using Trimmomatic (v0.39), which scanned reads from the 5′ end and discarded those shorter than 36 bases. The filtered reads in fastQ files were then aligned to the mouse reference genome (M26) with Ensembl v103 annotations using STAR (v2.6.1). Gene quantification was performed using RSEM (v1.3.1) in conjunction with STAR, both operating with default parameters [34–36]. For downstream analysis, normalized gene count data were generated using the DESeq2 normalization method, focusing on coding genes. Visualization of gene expression patterns, including heatmaps, was performed using R Packages (v4.4.0). Differential gene expression analysis was carried out using DESeq2 [37]. Genes with $|\log_2 FC|>0.5$, P value $< .05$ were selected. Volcano plots were generated using the R package ggplot2, with points colored based on P value and $\log_2$ fold-change cutoffs. Gene set enrichment analysis (GSEA) was performed using GSEA Software (v.4.3.2)[38, 39] . Gene Ontology (GO) analysis was conducted using the ICGC Data Portal (v6.3.3) (https://dcc.icgc.org/), with enrichment analysis performed against GO Molecular Function, GO Biological Process and GO cellular component, using a P value threshold of 0.01.

Replication stress signature scoring

Replication stress signature scoring using 21 GO pathways was performed as previously described [40]. DEGs were analyzed in relation to GO terms using the R package dnet. The replication stress signature was defined as genes that were differentially expressed at least 1.5-fold in RNA-seq and belonged to DDR and cell cycle control categories. For each selected GO term, differential expression was performed on TCGA-COAD, Cancer Cell Line Encyclopedia (CCLE), patient-derived, and mouse RNA-seq datasets. A composite measure, termed the Replication Stress Score, was generated by summing the individual scores from each selected GO pathway. The full list of GO pathways and corresponding genes is provided in Supplementary Table S2. Signature scores for each sample were computed using the genefu R package, which generates pathway-level scores based on predefined gene sets representing specific biological processes. This workflow was used to define the replication stress signature for each dataset. The same methodology was applied to bulk tumor datasets to compute replication stress scores in patient samples. Code

used for calculating the replication stress signature has been deposited in GitHub (https://github.com/nicesoung/NSMF).

Analysis of NSMF expression in relation to genomic instability across cancers

NSMF expression data (log-transformed FPKM + 1 values) and genomic instability metrics were analyzed across 4315 tumor samples representing multiple cancer types obtained from The Cancer Genome Atlas (TCGA). Genomic instability was quantified based on previously established genomic metrics, including telomeric allelic imbalance, frequency of large-scale genomic transitions, homologous recombination deficiency (HRD)-associated loss of heterozygosity (LOH) frequency, mutation burden per tumor, weighted genome integrity index, and overall LOH frequency, acquired from the publicly available dataset [41, 42]. Tumor samples were stratified into three categories—low (below 25th percentile), medium (between 25th and 75th percentile), and high (above 75th percentile)—for each genomic instability metric. Differences in NSMF expression levels among these stratified groups were statistically evaluated using unpaired *t*-tests.

Statistical analysis

Standard statistical tests are indicated in the figure legends of plots to which they apply. All plots were created using GraphPad Prism 8.0 software. Samples and experimental animals were randomly assigned to experimental groups. Male mice of the same age were randomly assigned to the various experimental groups. All data collection and analysis procedures were conducted without blinding to the experimental conditions. Sample collection was also randomized. Image acquisition and quantification were performed in a blinded manner. At least five randomly selected non-overlapping fields per sample were analyzed. Data are expressed as the mean ± SD or SEM, box-and-whiskers plot, or violin plot. Statistical significance was determined by a multiple unpaired two-tailed Student's *t*-test (for comparison between two groups), ordinary one-way analysis of variance (ANOVA) with Tukey's, Newman-Keuls, or Dunnett's test (for comparison among three or more groups), or a repeated measures two-way ANOVA followed by Tukey's test (for comparison among groups with multiple time points) using GraphPad Prism 8.0. No data point was excluded. $P < .05$ was considered statistically significant. Full P values are shown where appropriate.

Results

NSMF is upregulated and associated with replication stress in colorectal cancer

Replication stress arises from diverse sources and manifests in multiple forms, and the regulatory mechanisms vary considerably across different cellular contexts. Therefore, accurately quantifying replication stress using a limited set of markers remains challenging [40, 43, 44]. To overcome this limitation, recent studies developed transcription-based profiling methods integrating genes related to DNA maintenance, replication, and cell cycle regulation across 21 GO pathways (844 genes), effectively quantifying replication stress in pancreatic cancer (Supplementary Table S2) [40]. Using a similar profiling strategy, we assessed replication stress levels in CRC samples from TCGA and found significantly elevated replication stress scores compared to normal tissues, highlighting replication stress as a prominent feature in CRC (Supplementary Fig. S1A). Building on this observation, we designed a multi-step bioinformatics pipeline to systematically identify clinically relevant nuclear-localized factors that positively modulate replication stress to facilitate CRC progression (Fig. 1A). First, correlation analysis of replication stress scores was performed using RNA expression data derived from 483 colorectal adenocarcinoma patient samples from TCGA and 70 CRC cell lines from the CCLE. This initial analysis identified 3389 genes whose expression positively correlated with replication stress scores (average $r > 0.2$, $P < .05$). Subsequently, we excluded known DDR-related genes already included in the replication stress scoring. Next, differential expression analysis revealed 394 genes significantly upregulated in CRC tissues compared to normal counterparts (Log_2 FC > 0.5, $P < .05$). Among these candidates, we further prioritized 17 genes whose elevated expression was significantly associated with poor clinical prognosis (Fig. 1A). Notably, four of these genes, SNAI1, PAK6, YEATS2, and MORC2, have been previously implicated in DNA damage regulation pathways in various cancers [45–48]. Of particular interest, NSMF emerged as a strong candidate, exhibiting significantly elevated expression in CRC tissues relative to normal colon tissues, and its expression was positively correlated with replication stress scores (Fig. 1B and C; Supplementary Fig. S1B). Analysis of 30 cancer cell types from the CCLE database confirmed that CRC cells had the highest NSMF expression levels among cancer cell types examined (Supplementary Fig. S1C). And protein-level validation by western blot analysis confirmed that NSMF expression was substantially higher in CRC cell lines compared to the normal colon fibroblast line, CCD-18Co (Supplementary Fig. S1D). Importantly, elevated NSMF expression was not limited to CRC but was also observed broadly across other malignancies, including breast, lung, kidney, prostate, and melanoma, compared to their respective normal tissues (Supplementary Fig. S1E). Consistently, higher NSMF expression was significantly associated with poorer overall survival not only in CRC but also in breast and lung cancer patients (Fig. 1D and Supplementary Fig. S1F). Notably, the increase in NSMF expression emerged as early as stage I and persisted across all CRC stages (Fig. 1E). Furthermore, high NSMF expression in early-stage tumors (stage I–II), rather than in late-stage tumors (stage III–IV), was more strongly associated with poor patient prognosis, suggesting that NSMF induction occurs early during tumorigenesis and may play an important role in CRC development and progression (Supplementary Fig. S1G). To experimentally validate these bioinformatics findings, we performed qRT-PCR in 36 paired CRC patient samples. NSMF messenger RNA (mRNA) levels were significantly elevated in 33 of the tumor samples compared with their matched adjacent normal tissues (Fig. 1F). In addition, RNA sequencing analyses of an additional five paired CRC samples confirmed increased NSMF expression together with higher replication stress scores in tumor tissues, revealing a strong positive correlation between the two parameters (Fig. 1G–I). NSMF expression was higher in deficient MMR tumors than in proficient mismatch repair (pMMR) tumors, which are characterized by greater genomic instability (Supplementary Fig. S1H). Consistent with these transcriptomic findings, western blot analysis demonstrated markedly higher NSMF protein levels in CRC tissues, accompanied by increased expression of the DNA damage marker

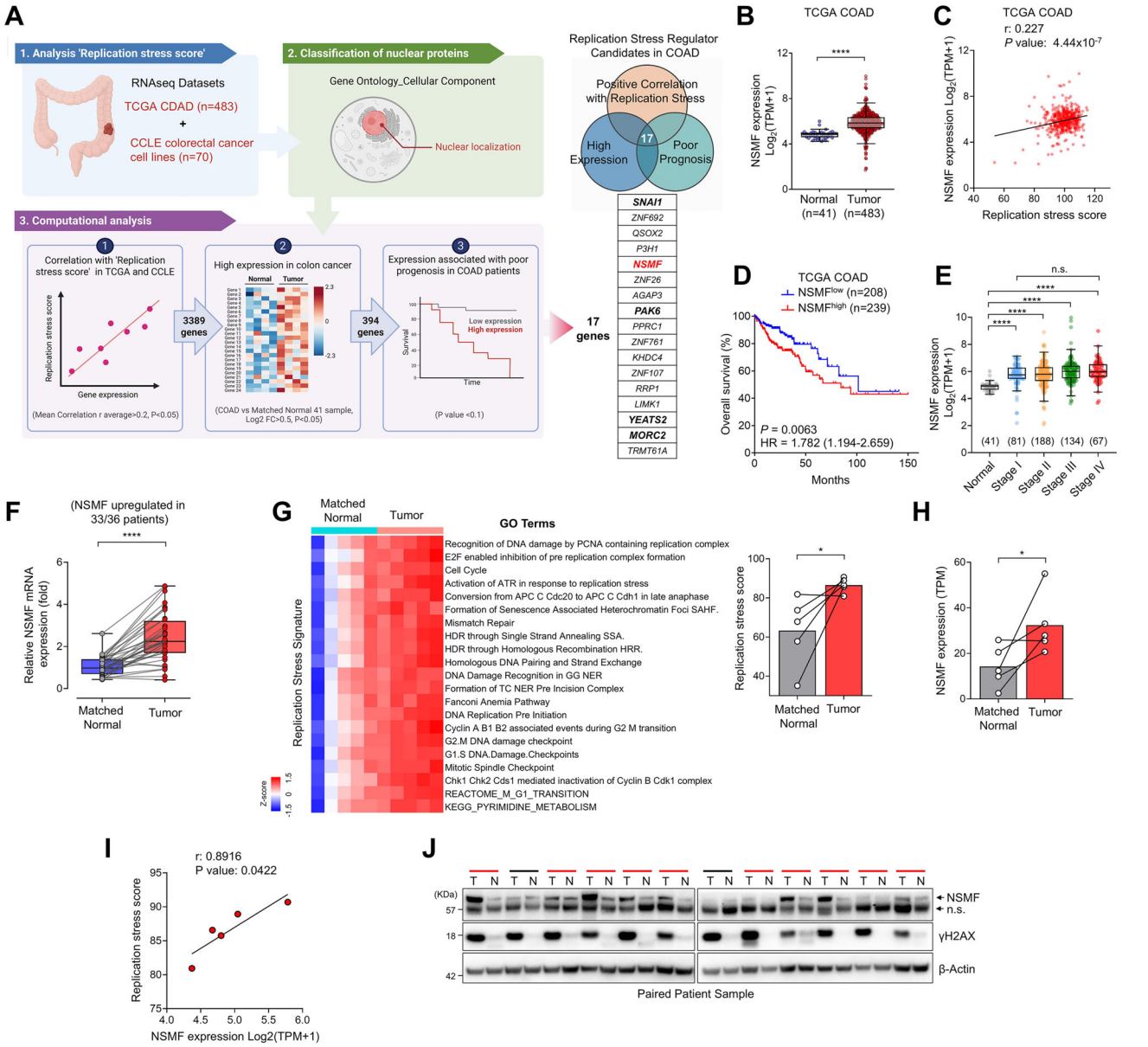

Figure 1. NSMF expression correlates with replication stress and poor prognosis in CRC. (**A**) Schematic workflow for identifying candidate genes modulating replication stress to promote CRC progression. Seventeen candidate genes were selected based on positive correlation with replication stress score, elevated expression in tumors versus normal tissues, and association with poor prognosis. (**B**) NSMF mRNA expression in normal ($n = 41$) and tumor samples ($n = 483$) from TCGA-COAD dataset. Data are represented as box and whiskers plots using Tukey's method or before-after plot. $^{****}P < .0001$, unpaired two-tailed Student's *t*-test. (**C**) Correlation between NSMF expression and replication stress score in TCGA-COAD dataset. (**D**) Kaplan–Meier survival analysis of COAD patients stratified by NSMF expression level. (**E**) NSMF mRNA expression across pathological stages in TCGA-COAD dataset. Data are represented as box and whiskers plots using Tukey's method. $^{****}P < .0001$, n.s., not significant, one-way ANOVA followed by Tukey's HSD test. (**F**) qRT-PCR of NSMF mRNA level in matched normal-tumor pairs of 36 CRC patients. Data are represented as box and whiskers plots using Min to Max method. $^{****}P < .0001$, unpaired two-tailed Student's *t*-test. (**G–I**) RNA-seq analysis of five matched normal–tumor pairs from CRC patients. (**G**) Heatmap of DDR and cell cycle control gene sets used to compute replication stress score, showing upregulation in tumors. (**H**) Higher NSMF expression in tumors versus matched normals. (**I**) Positive correlation of NSMF expression with replication stress scores. $^{*}P < .05$, unpaired two-tailed Student's *t*-test. (**J**) Immunoblot for NSMF and γH2AX proteins in paired normal (**N**) and tumor (**T**) CRC samples ($n = 12$). Red highlights pairs indicate increased NSMF protein in tumors, quantified relative to β-actin by ImageJ.

γH2AX compared with adjacent normal tissues (Fig. 1J). Collectively, these results demonstrate that NSMF is upregulated in cancer tissues and strongly correlates with elevated replication stress, supporting the notion that NSMF functions as an important regulator that may promote cancer progression by modulating replication stress.

Nsmf depletion suppresses colorectal tumorigenesis in *Apc*$^{Min/+}$ mice

Tight regulation of DNA replication and cell proliferation is essential for normal development and physiological homeostasis. Accordingly, complete knockout of genes involved in DNA replication and repair typically results in embryonic lethality or severe developmental defects. To investigate the physiological roles of NSMF *in vivo*, we generated and char-

acterized complete *Nsmf* knockout mice. Efficient deletion of NSMF in intestinal tissues was confirmed by qRT-PCR and western blot analyses (Supplementary Fig. S2A and B). Consistent with previous studies [49], *Nsmf* knockout mice remained viable and fertile, exhibited normal litter sizes, Mendelian inheritance ratios among homozygous (−/−), heterozygous (+/−), and wild-type (WT, +/+) offspring and showed no detectable physiological abnormalities in body size, weight, lifespan, or intestinal histology (Supplementary Fig. S2C-E). Ki-67 staining further indicated normal proliferation in intestinal crypts, demonstrating that NSMF is dispensable for maintaining intestinal epithelial homeostasis (Supplementary Fig. S2F).

Next, to determine the role of NSMF specifically in colorectal tumorigenesis, we crossed $Nsmf^{-/-}$ mice with $Apc^{Min/+}$ mice, a widely-used CRC model characterized by spontaneous intestinal adenoma formation due to truncating mutations in the *Apc* gene, similar to human CRCs [50]. Interestingly, γH2AX levels were markedly elevated only in regions that had developed into tumors, not in adjacent normal intestinal tissues (Fig. 2A). Likewise, *Nsmf* expression was specifically upregulated in these tumor-derived regions from $Apc^{Min/+}$ mice (Fig. 2B). Despite no obvious effects on normal intestinal tissues, *Nsmf* deficiency significantly suppressed adenomatous polyp formation (>0.3 mm in diameter) in the small intestines of $Apc^{Min/+}$ mice (Fig. 2C–E). Importantly, *Nsmf*-deficient $Apc^{Min/+}$ mice exhibited significantly prolonged median survival (59 days longer) compared to control $Nsmf^{+/+}$; $Apc^{Min/+}$ mice, indicative of delayed cancer progression and improved clinical outcomes (Fig. 2F). To understand the mechanisms underlying reduced tumorigenesis, we analyzed tumor proliferation and apoptosis markers. Tumors from *Nsmf*-deficient mice exhibited significantly decreased Ki-67 staining compared to controls, demonstrating reduced tumor cell proliferation. In contrast, apoptosis, as indicated by cleaved caspase-3 staining, was not significantly altered, suggesting NSMF primarily supports tumor proliferation without significantly affecting apoptosis (Fig. 2G and H).

Finally, to further validate these findings, we utilized an *ex vivo* intestinal organoid model [51]. Small intestinal crypts isolated from $Nsmf^{+/+}$ and $Nsmf^{-/-}$ mice successfully developed into normal enteroids, characterized by stem cell-rich budding crypt structures, confirming normal epithelial cell proliferation in the absence of NSMF. However, when isolated from $Nsmf^{+/+}$; $Apc^{Min/+}$ mice, organoids progressively developed into tumor spheroids during successive passages. In contrast, organoids from $Nsmf^{-/-}$; $Apc^{Min/+}$ mice showed significantly impaired tumor spheroid formation, predominantly retaining normal enteroid structures (Fig. 2I). Collectively, these data robustly demonstrate that NSMF is essential for colorectal tumor initiation and proliferation *in vivo*, with minimal or no detectable impact on normal intestinal epithelial homeostasis.

Increased replication stress and DNA damage in intestinal tumors of *Nsmf* knockout mice

To investigate the molecular consequences of NSMF deficiency in colorectal tumorigenesis, we analyzed mRNA expression profiles in intestinal adenomas and adjacent normal tissues from $Apc^{Min/+}$ mice with and without *Nsmf* deletion. Adenomas from $Nsmf^{-/-}$; $Apc^{Min/+}$ mice showed substantial changes in gene expression compared to adenomas from $Nsmf^{+/+}$ mice, whereas adjacent normal tissues exhibited minimal differences (Fig. 3A). This suggests that *Nsmf* deletion has a more pronounced impact on tumor tissues than on surrounding normal tissues. Using criteria of Log_2 FC > 0.5 ($P < .05$), we identified 5579 differentially expressed genes (DEGs) in $Nsmf^{-/-}$ adenomas, including 3337 upregulated and 2242 downregulated genes. In contrast, adjacent normal tissues showed only 1588 DEGs, indicating that NSMF loss predominantly affects tumor tissue (Fig. 3B). Gene Ontology Biological Process (GO-BP) analysis of these DEGs revealed significant enrichment in pathways associated with DDR, including DNA repair, cellular response to DNA damage stimuli, and ionizing radiation (Fig. 3C and Supplementary Fig. S3A). Further, GSEA highlighted strong activation of replication stress and DNA damage related pathways in tumors lacking NSMF compared to WT tumors (Fig. 3D and Supplementary Fig. S3B). Notably, replication stress scores were significantly elevated in adenomas of $Nsmf^{-/-}$ mice compared to their WT counterparts (Fig. 3E). Given the known role of NSMF in replication stress regulation, we hypothesized that NSMF deficiency impairs replication stress resolution, resulting in increased DNA damage in tumor tissues. To test this, we performed IHC staining for γH2AX in intestinal tumor sections. Tumors from $Nsmf^{-/-}$ mice exhibited significantly higher γH2AX staining than those from $Nsmf^{+/+}$; $Apc^{Min/+}$ mice, indicating elevated DNA damage (Fig. 3F). Collectively, these results indicate that NSMF critically modulates replication stress during colorectal tumorigenesis, protecting tumor cells from excessive DNA damage and maintaining tumor growth.

NSMF depletion impairs colorectal cancer cell proliferation

Analysis of 70 human CRC samples revealed a significant positive correlation between NSMF expression levels and replication stress scores (Fig. 4A and Supplementary Fig. S4A). Knockdown of NSMF in HCT116 and SW480 cells led to a marked reduction in cell proliferation and colony-forming ability (Fig. 4B and C; Supplementary Fig. S4B). Similar growth-inhibitory effects were observed upon NSMF depletion in additional CRC cell line, including SW620, SNU-407, and RKO (Fig. 4D). Beyond CRC, NSMF knockdown also reduced cell proliferation in the lung cancer cell line PC9 and the breast cancer cell line MDA-MB-231 (Supplementary Fig. S4C). Because replication stress is known to impair cell-cycle progression, we next examined the cell-cycle profiles of NSMF-depleted CRC cells. Loss of NSMF led to aberrant cell-cycle distribution, characterized by an accumulation of cells in the G1 phase and a corresponding decrease in the S-phase population (Fig. 4E). These findings confirm NSMF as essential for cancer cell proliferation by facilitating proper cell cycle progression.

NSMF regulates the replication stress repair pathway to prevent DNA damage in CRC

To determine whether NSMF modulates CRC cell proliferation by regulating replication stress, we performed a DNA fiber assay to directly assess its role in DNA replication fork progression. Cells were sequentially labeled with the thymidine analogs chlorodeoxyuridine (CldU) and iododeoxyuridine (IdU) to visualize replication dynamics. In NSMF-knockdown HCT116 cells, the lengths of CldU- and IdU-labeled replication tracts were significantly shorter than in control cells, indicating impaired replication fork progression

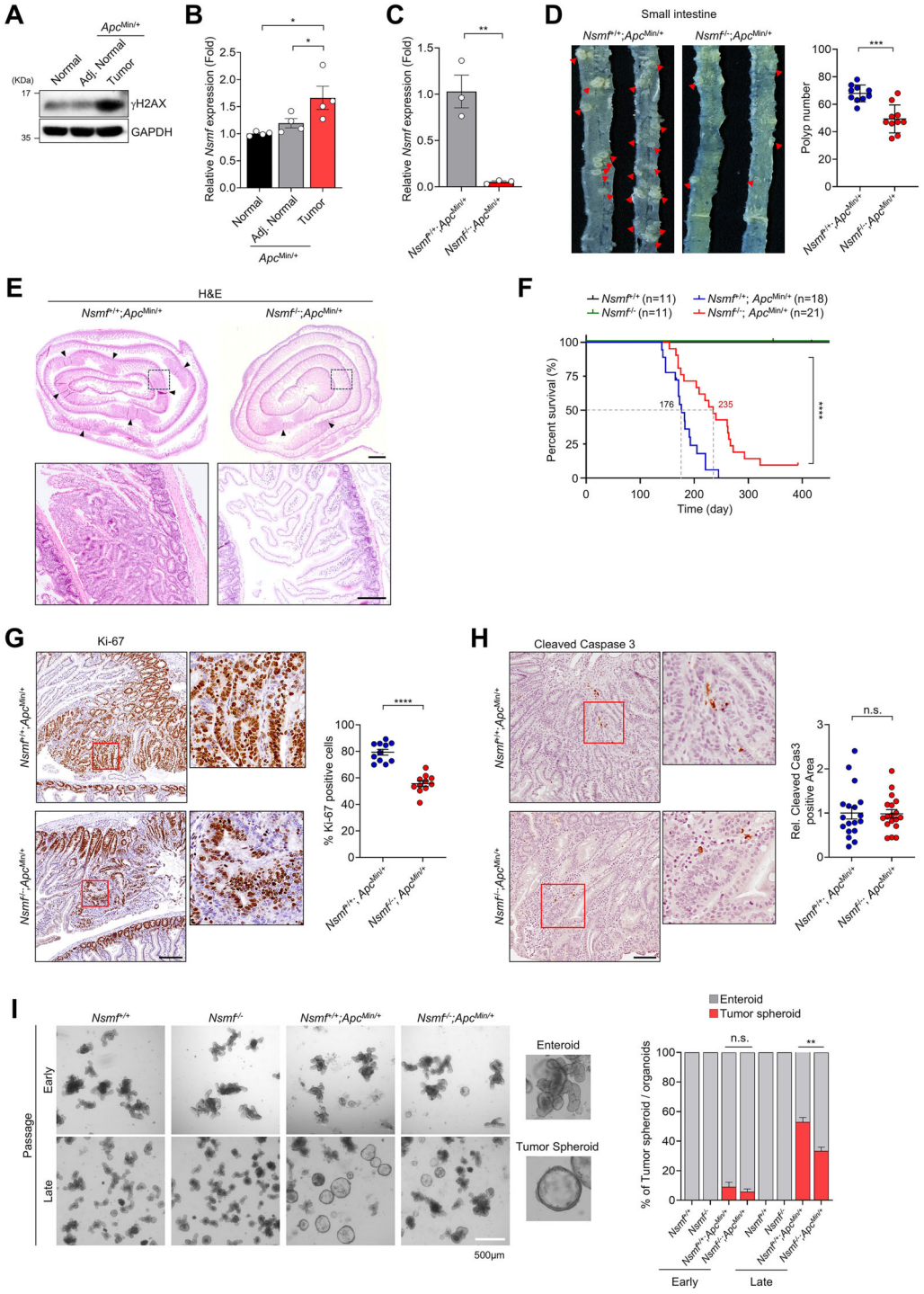

Figure 2. NSMF knockout inhibits intestinal tumorigenesis in $Apc^{Min/+}$ mice. (**A**) Immunoblot of γH2AX expression in normal, adjacent normal (Adj. Normal), and tumor tissue from $Apc^{Min/+}$ mice. GAPDH served as a loading control. (**B**) Relative *Nsmf* mRNA in intestinal tissue from APC WT (normal), adjacent normal intestinal tissue (adjacent normal), and intestinal tumors (tumor) from $Apc^{Min/+}$ mice. Data represent the mean ± SEM ($n = 4$ mice per group). $*P < .05$, one-way ANOVA followed by Newman–Keuls test. (**C**) qRT-PCR validation of *Nsmf* knockout efficiency in adenomas. Data represent the mean ± SEM ($n = 3$ mice per group). $**P < .01$, unpaired two-tailed Student's *t*-test. (**D**) Representative images of small intestines from 140-day-old $Nsmf^{+/+}$; $Apc^{Min/+}$ and $Nsmf^{-/-}$; $Apc^{Min/+}$ mice (left). Tumor counts are quantified (right). Data represent the mean ± SD ($n = 10$ mice per group). $***P < .001$, unpaired two-tailed Student's *t*-test. (**E**) H&E staining of intestinal swiss-roll sections from $Nsmf^{+/+}$; $Apc^{Min/+}$ and $Nsmf^{-/-}$; $Apc^{Min/+}$ mice. Scale bar, 1 mm (top), 200 μm (bottom). (**F**) Kaplan–Meier survival curves of $Nsmf^{+/+}$, $Nsmf^{-/-}$, $Nsmf^{+/+}$; $Apc^{Min/+}$ and $Nsmf^{-/-}$; $Apc^{Min/+}$ mice. Median survival rates of $Nsmf^{+/+}$; $Apc^{Min/+}$ and $Nsmf^{-/-}$; $Apc^{Min/+}$ mice are 176 and 235 days respectively. $****P < .0001$. Expression of Ki-67 (**G**) and cleaved caspase 3 (**H**) in tumors from $Nsmf^{+/+}$; $Apc^{Min/+}$ and $Nsmf^{-/-}$; $Apc^{Min/+}$ mice detected by immunohistochemistry (IHC). Statistical analyses of Ki-67 positive cells and cleaved caspase 3 positive areas in tumors ($n = 4$ mice per group, 2–5 images analyzed per mouse). Scale bars, 200 and 100 μm, respectively. Data represent the mean ± SEM. $****P < .0001$, n.s., not significant, unpaired two-tailed Student's *t*-test. (**I**) Bright-field microscopy images of intestinal organoid and percentage of tumor spheroid of $Nsmf^{+/+}$, $Nsmf^{-/-}$, $Nsmf^{+/+}$; $Apc^{Min/+}$, and $Nsmf^{-/-}$; $Apc^{Min/+}$ at early and late passages. Scale bar, 500 μm. Error bars indicate mean ± SEM. $****P < .0001$, n.s., not significant, one-way ANOVA followed by Tukey's HSD test. ($n = 3$ independent organoid lines; minimum six images per genotype).

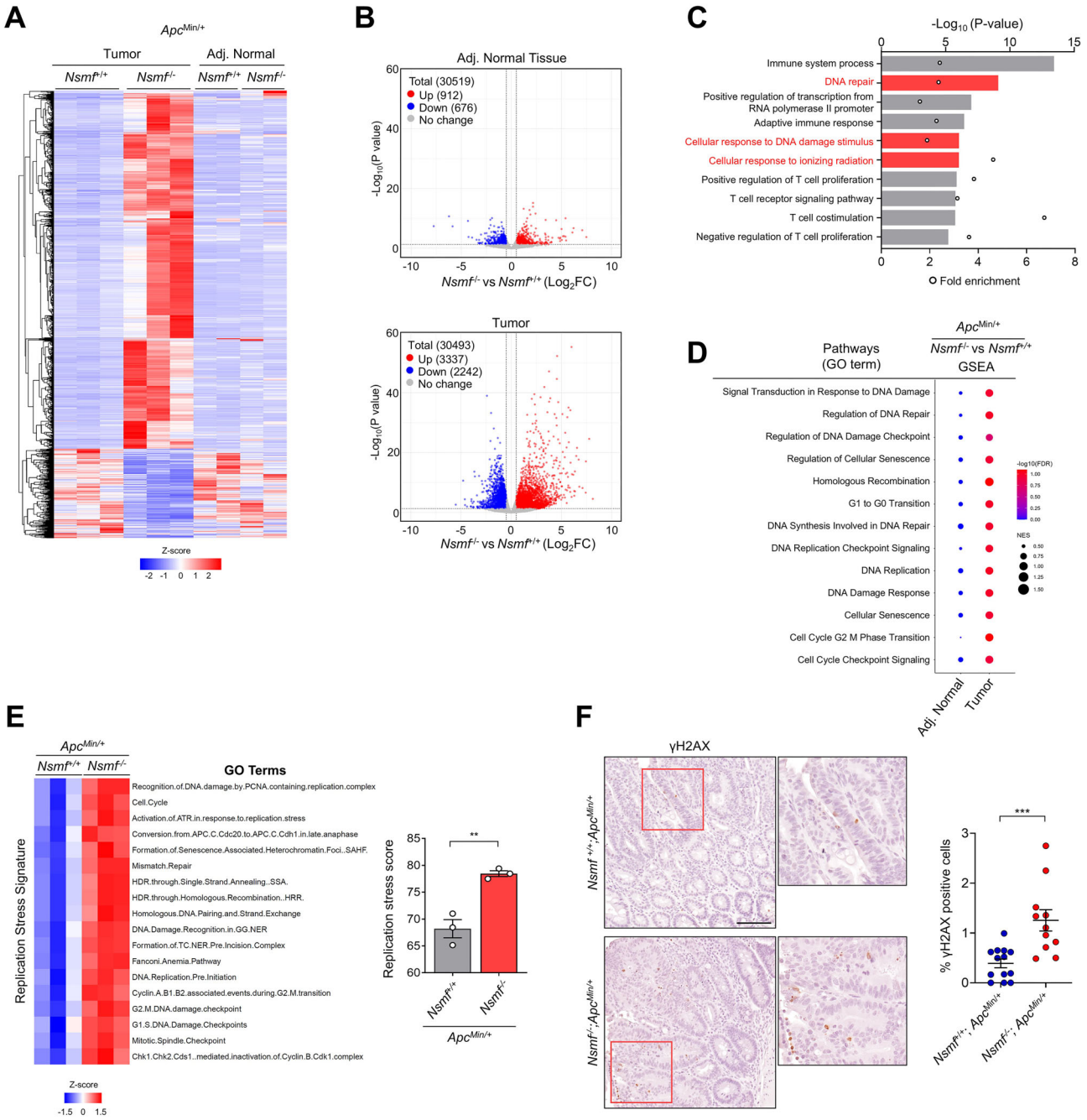

Figure 3. NSMF knockout induces replication stress and DNA damage in intestinal tumors. (**A**) RNA sequencing analysis was performed using adjacent normal intestinal tissue and tumor from *Nsmf*$^{+/+}$; *Apc*$^{Min/+}$ and *Nsmf*$^{-/-}$; *Apc*$^{Min/+}$ mice. Heatmap depicting the hierarchical clustering results of the DEGs. (Tumor, $n = 3$ mice per genotypes; Adj.Normal, $n = 2$ mice per genotypes). (**B**) Volcano plots showing DEGs in adjacent normal tissues (top) and tumor tissues (bottom) comparing *Nsmf*$^{+/+}$; *Apc*$^{Min/+}$ versus *Nsmf*$^{-/-}$; *Apc*$^{Min/+}$ mice. Dotted lines indicate statistical significance threshold ($P < .05$) and expression fold-change cutoff ($|\text{Log}_2\text{FC}| > 0.5$). Red represents up-regulated expression, blue represents down-regulated expression. (**C**) The top 10 enriched GO biological process terms for the upregulated DEGs in the tumor of *Nsmf*$^{-/-}$; *Apc*$^{Min/+}$ mice were identified using the DAVID functional annotation database, with DNA damage-related terms highlighted in red. The ranking is based on *P*-values, indicating statistical significance. (**D**) GSEA analysis comparing DNA damage-related pathway enrichment between *Nsmf*$^{+/+}$; *Apc*$^{Min/+}$ and *Nsmf*$^{-/-}$; *Apc*$^{Min/+}$, analyzed separately in adjacent normal and tumor tissues. (**E**) Heatmap visualization of replication stress signature in tumor tissues from *Nsmf*$^{+/+}$; *Apc*$^{Min/+}$ and *Nsmf*$^{-/-}$; *Apc*$^{Min/+}$. Corresponding replication stress score presented as bar graph. Data represent the mean ± SEM. $**P < .01$, unpaired two-tailed Student's *t*-test ($n = 3$ mice per genotype). (**F**) Representative IHC images of γH2AX in tumors from *Nsmf*$^{+/+}$; *Apc*$^{Min/+}$ and *Nsmf*$^{-/-}$; *Apc*$^{Min/+}$ mice, with quantification of the percentage of γH2AX-positive cells relative to *Nsmf*$^{+/+}$; *Apc*$^{Min/+}$ (right). Scale bar, 100 μm. Data represent the mean ± SEM. $***P < .001$, unpaired two-tailed Student's *t*-test ($n = 4$ mice per genotype, 2–4 independent images per mouse).

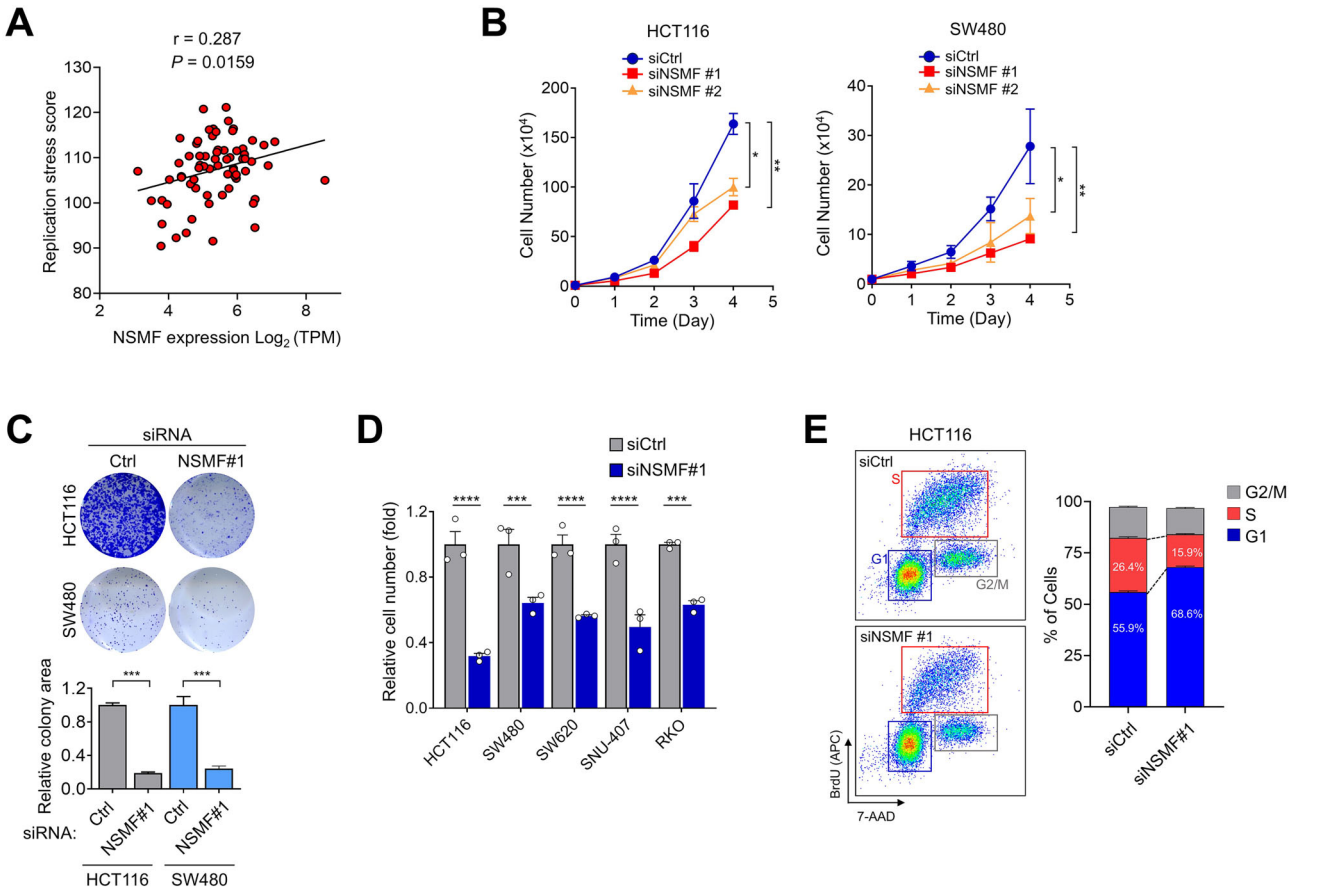

Figure 4. NSMF knockdown inhibits CRC cell proliferation and cell-cycle progression (**A**) Correlation analysis between NSMF expression and replication stress score in CRC cell line from CCLE dataset. (**B**) Cell growth curves of HCT116 and SW480 cells following transfection with control or NSMF siRNAs over 5 days, measured by direct cell counting ($n = 3$). Data represent the mean ± SD. ****$P < .0001$, two-way ANOVA with repeated measures, followed by Tukey's multiple comparisons test. (**C**) Colony formation assay showing the effect of NSMF knockdown in HCT116 and SW480 cells. Representative images (upper panel) and quantification of colonies area (lower panel) are shown. Data represent mean ± SD. ***$P < .001$, unpaired two-tailed Student's *t*-test (HCT116, $n = 2$; SW480, $n = 3$). (**D**) Relative cell number of five CRC cell lines (HCT116, SW480, SW620, SNU-407, and RKO) measured 3 days after NSMF knockdown compared to control. Data represent the mean ± SEM. ($n = 3$) ***$P < .001$, ****$P < .0001$, unpaired two-tailed Student's *t*-test. (**E**) Cell-cycle analysis by flow cytometry in HCT116 cells transfected with siCtrl or siNSMF#1. Representative flow cytometry plots (left) and quantification of cell cycle distribution in G1, S, and G2/M phases with percentages indicated in bar graph (right). Data are presented as the mean ± SD ($n = 3$). All experiments were independently performed at least three times, and representative results are shown.

(Fig. 5A). To evaluate replication fork recovery, cells were treated with hydroxyurea (HU) for 2 h to stall replication forks, followed by a 30-min IdU pulse. The IdU-labeled tracts were markedly shorter in NSMF-depleted cells than in controls (Fig. 5B). Moreover, NSMF-deficient cells showed a pronounced increase in newly fired replication forks (IdU-only) as well as stalled forks (CldU-only), indicating that loss of NSMF promotes compensatory dormant origin firing while simultaneously compromising fork stability and recovery under replication stress (Fig. 5C and D). These results indicate that NSMF deficiency disrupts replication fork stability and recovery in CRC cells. To further investigate NSMF's role in replication stress regulation, we analyzed cell-cycle progression in NSMF-depleted cells synchronized in early S phase via HU treatment. Following HU removal, NSMF-deficient cells displayed markedly delayed cell-cycle progression, characterized by a slower transition from early to late S phase and a delayed G1-to-S entry, indicating inefficient resolution of replication stress (Fig. 5E and Supplementary Fig. S5C). Previously, we demonstrated that NSMF translocates to DNA damage sites and stabilizes the RPA complex under replication stress. Consistent with this, replication stress in HCT116 and SW480 CRC cells triggered the recruitment of RPA, NSMF, and γH2AX to chromatin. Cytochemical analysis further confirmed that NSMF colocalized with γH2AX following HU treatment (Supplementary Fig. S5A and B). In HCT116 cells, phosphorylated RPA foci accumulated upon HU treatment; however, stable NSMF knockdown cells exhibited impaired RPA phosphorylation, leading to defective formation of RPA foci under replication stress conditions (Fig. 5F and Supplementary Fig. S5D). Similarly, in tumor from $Apc^{Min/+}$ mice, NSMF depletion led to a reduction in ATR signaling pathway activity, including decreased phosphorylation of ATR, RPA, and CHK1 (Supplementary Fig. S5E). Given RPA's role in stabilizing ssDNA and protecting stalled replication forks, these findings suggest that NSMF loss exacerbates DNA damage under replication stress conditions. To confirm this, we assessed DNA damage levels in NSMF-depleted cells. NSMF knockdown impaired RPA phosphorylation, and HU treatment further increased γH2AX foci, indicating elevated DNA damage; however, re-expression of NSMF reduced these γH2AX levels (Supplementary Fig. S5F). Following HU

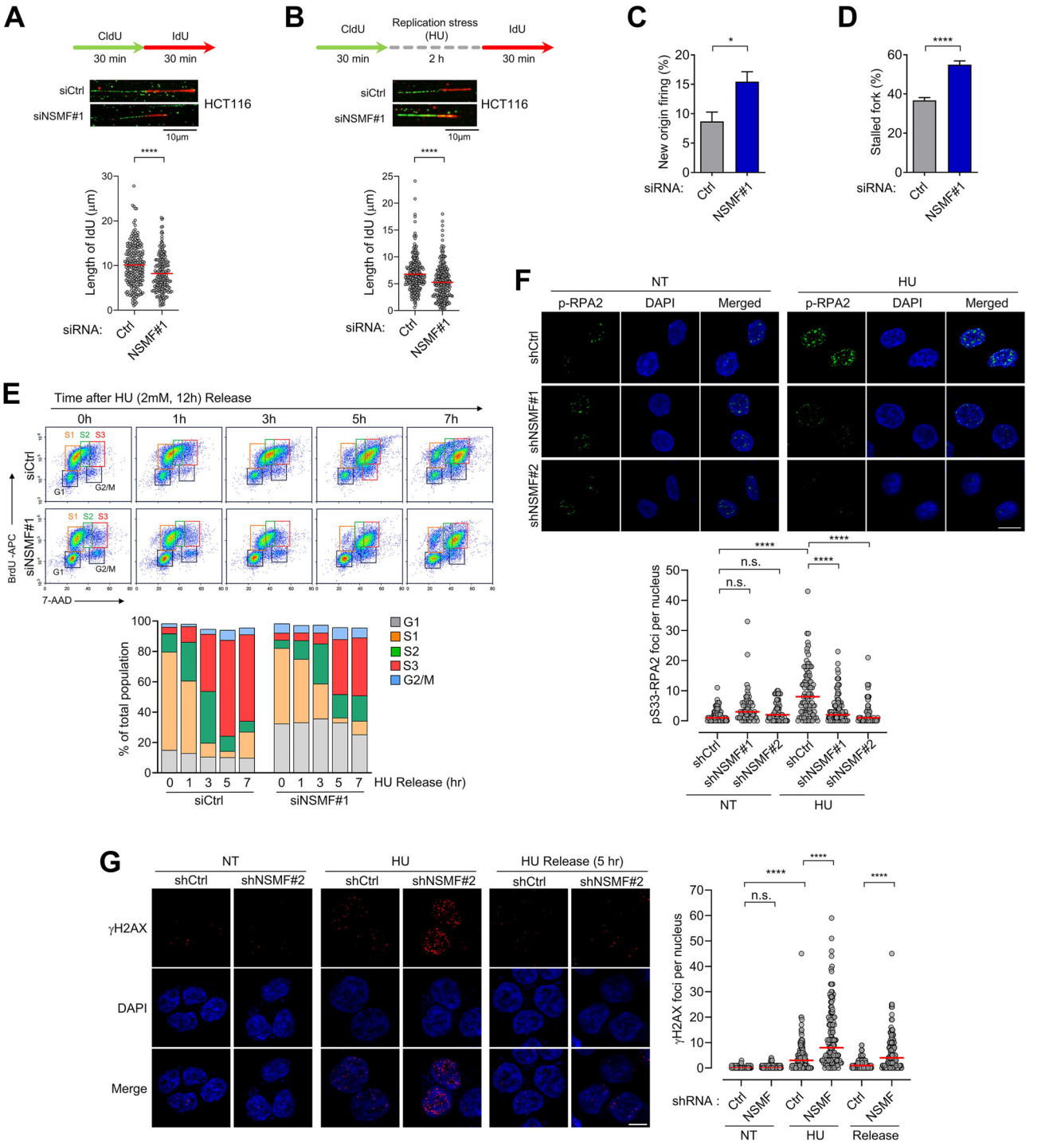

Figure 5. NSMF depletion affects DNA replication dynamics and induces replication stress. **(A, B)** DNA fiber analysis examining the effect of NSMF on replication dynamics in HCT116 cells. For normal conditions, cells were sequentially labeled with CldU and IdU for 30 min each (**A**). For replication stress conditions, cells were treated with 2 mM hydroxyurea (HU) for 2 h between CldU and IdU pulses (**B**). Representative DNA fiber images (upper) and quantification of IdU tract lengths (lower). The median value is indicated, derived from the analysis of 200 or more IdU and CldU tracts per experimental condition. $****P < .0001$, two-tailed Mann–Whitney test. (**C**, **D**) Quantification of newly fired origins (C, IdU-only fibers) and stalled forks (D, CldU-only fibers) in HCT116 cells transfected with siCtrl or siNSMF#1. A total of 300–350 fibers from 7 to 18 randomly selected non-overlapping images per condition were analyzed. Data represent mean ± SEM. $*P < .05$, $****P < .0001$. Statistical significance was assessed using a Mann–Whitney test. Results are representative of three independent experiments. (**E**) BrdU pulse-chase analysis of cell-cycle kinetics in HCT116 cells transfected with siCtrl or siNSMF#1 following release from a HU block (2 mM, 12 h). Representative results from three independent experiments are shown. (**F**) Immunofluorescence analysis of phospho-RPA2 foci in control (shCtrl) and NSMF-depleted (shNSMF#1 and #2) HCT116 cells under normal (NT) or HU treatment (2 mM, 16 h) conditions. The number of phospho-RPA2 foci per cell was quantified from at least 54 cells across two independent experiments. Scale bar, 10 μm. Data are presented as median. $*P < .05$, $****P < .0001$, n.s., not significant, Kruskal–Wallis test followed by Dunn's multiple comparisons test. (**G**) γH2AX staining for control (shCtrl) or NSMF-depleted (shNSMF#2) HCT116 cells treated with HU treatment (2 mM, 16 h), and directly fixed or allowed to grow in the complete medium for 5 h in the absence of HU. The number of γH2AX foci per cell was quantified from at least 106 cells across three independent experiments. Scale bar, 10 μm. Data are presented as median. $****P < .0001$, n.s., not significant, Kruskal–Wallis test followed by Dunn's multiple comparisons test.

removal, γH2AX clearance was notably delayed in NSMF-deficient cells, suggesting impaired replication stress recovery and heightened DNA damage accumulation (Fig. 5G). Furthermore, NSMF knockdown significantly sensitized HCT116 cells to PARP inhibition (Olaparib) and to ATR (VE-821) and CHK1 (Rabusertib) inhibitors, whereas no sensitization was observed upon treatment with the DNA-damaging agents cisplatin or doxorubicin (Supplementary Fig. S5G). These results demonstrate that NSMF is essential for maintaining replication fork stability, facilitating replication stress recovery, and preventing severe DNA damage in CRC cells.

NSMF prevents excessive replication stress-induced senescence to sustain tumor progression

Persistent and unresolved replication stress can lead to irreparable DNA damage, culminating in apoptosis or senescence. In line with our observation that NSMF depletion does not induce tumor cell death *in vivo*, NSMF knockdown in HCT116 cells did not induce apoptosis, as demonstrated by unchanged levels of apoptotic markers including cleaved PARP, caspase-3, and annexin V staining (Supplementary Fig. S6A and B). Nevertheless, NSMF-knockdown HCT116 cells exhibited distinct characteristics of cellular senescence, evidenced by increased SA-β-gal activity and altered cell morphology (Fig. 6A). Consistently, primary MEFs derived from *Nsmf*$^{-/-}$ mice demonstrated reduced proliferation and significantly higher numbers of SA-β-gal-positive cells by passage six compared to wild-type MEFs (Supplementary Fig. S6C and D). RNA sequencing analysis of tumor tissues from *Nsmf*$^{-/-}$; *Apc*$^{Min/+}$ mice revealed elevated expression of cellular senescence markers and SASP genes relative to *Nsmf*$^{+/+}$; *Apc*$^{Min/+}$ mice (Fig. 6B). qRT-PCR validation further confirmed increased expression of p16, p19, and various SASP-related factors, such as IL-1α, IL-1β, IL-6, IL-8, CCL2, CCL20, MMP3, and SerpinE1 in *Nsmf*$^{-/-}$; *Apc*$^{Min/+}$ tumors (Fig. 6C). Western blot analysis reinforced these observations, showing increased levels of p16 and p21 proteins, indicating that NSMF deficiency inhibits tumor growth through enhanced cellular senescence (Fig. 6D). Typically, oncogene activation or tumor suppressor loss induces replication stress-mediated growth arrest and senescence in normal cells, serving as a barrier against tumor progression [19, 52, 53]. To assess whether NSMF mitigates oncogene-induced senescence, we utilized an oncogene-induced senescence model in IMR90 fibroblasts [54, 55]. Cells were transduced to express Ras^{G12V}, NSMF, or both (Fig. 6E). NSMF overexpression alone did not impact IMR90 cells; however, Ras^{G12V} expression increased cyclin D1 (a cell-cycle progression marker), γH2AX accumulation, p16 expression, and SA-β-gal-positive cell frequency. In contrast, co-expression of NSMF with Ras^{G12V} significantly reduced SA-β-Gal staining and decreased p16 and γH2AX levels (Fig. 6F and G). Moreover, NSMF co-expression suppressed the Ras^{G12V}-induced upregulation of senescence-related genes (Supplementary Fig. S6E). Cytochemical analysis further supported these findings, demonstrating that while Ras^{G12V} expression markedly increased γH2AX foci, NSMF co-expression notably reduced these foci (Fig. 6H). Since appropriate levels of replication stress can induce genomic instability, we examined whether NSMF's precise regulation of replication stress limits excessive DNA damage and senescence, potentially enhancing genomic instability in cancer. Analysis of the TCGA database across multiple cancer types revealed that high chromosomal instability—indicated by telomeric allelic imbalance, LOH, large-scale transitions, mutations, and a weighted genome integrity index—significantly correlated with elevated NSMF expression (Fig. 6I). Collectively, these findings suggest that NSMF finely tunes replication stress to avoid severe DNA damage and cellular senescence, ultimately promoting genomic instability and facilitating tumor progression (Fig. 6J).

Discussion

Mutations acquired during cell division contribute to approximately two-thirds of genetic alterations in human cancers, indicating the critical role of replication-associated errors in tumor initiation and progression [56]. In the early stages of tumorigenesis, replication stress-induced genomic instability, coupled with the selective inactivation of key DDR factors such as TP53 and ATM, establishes a permissive environment for tumorigenesis. As tumors progress, this instability continues to propel cancer advancement, leading to metastasis and drug resistance [57]. Traditionally, genomic instability was thought to progressively increase with cancer progression. However, paradoxically, several replication stress-related genes—generally considered tumor suppressors—are frequently upregulated in cancers, suggesting cancer cells must carefully balance beneficial genomic instability against excessive DNA damage that threatens their viability [58]. In particular, oncogene activation or tumor suppressor loss induces replication stress, triggering apoptosis or senescence, and thus establishing a critical barrier against early tumor progression [53, 59–61]. Therefore, cancer cells must have evolved sophisticated mechanisms to precisely regulate replication stress, maintaining it within a threshold that allows genomic instability while supporting continuous proliferation and tumor growth [9]. Despite its recognized importance, the precise mechanisms by which cancer cells adapt to and manage excessive replication stress remain largely unclear.

In our study, we identified NSMF as a crucial regulator of excessive replication stress that supports the development and progression of CRC. By integrating bioinformatics analyses of patient datasets with functional studies in cell lines and *in vivo* models, we demonstrate that NSMF promotes replication fork progression under stress conditions, mitigates replication stress-induced DNA damage, and ultimately sustains tumor cell proliferation. Furthermore, our findings regarding NSMF's association with increased chromosomal instability suggest that, unlike most DDR genes whose inactivation typically enhances genomic instability, precise modulation of replication stress can also promote genomic instability (Fig. 6J). These findings demonstrate the importance of mechanisms that finely regulate replication stress within a tolerable range, highlighting their potential as novel targets for controlling tumor initiation and growth.

Our findings reveal that NSMF expression is significantly elevated in CRC tissues compared to normal colon epithelium and is strongly associated with increased replication stress and poor patient prognosis (Fig. 1B–I). In *Apc*$^{Min/+}$ mice, NSMF expression was upregulated in adenoma tissue compared to normal tissue carrying the same *Apc* mutation, coinciding with an increase in γH2AX levels (Fig. 2A and B). This suggests that NSMF is required for proliferating cells experiencing increased replication stress. Similarly, in human CRC tis-

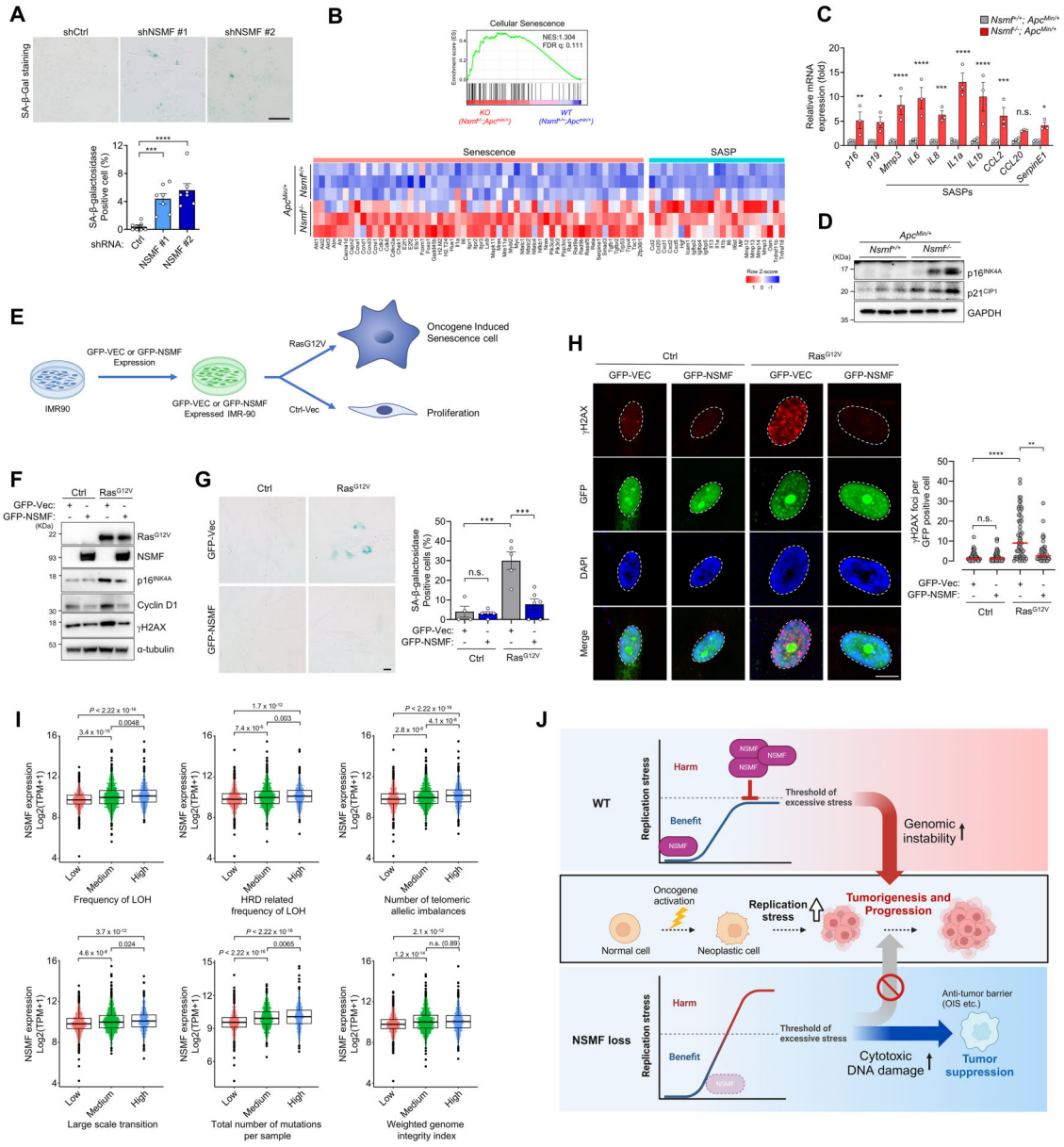

Figure 6. NSMF mitigates replication stress and prevents oncogene-induced senescence. (**A**) SA-β-galactosidase (SA-β-Gal) staining in stable NSMF knockdown (shNSMF #1 and #2) or control (shCtrl) HCT116 cells. Representative images (upper) and quantification of SA-β-gal positive cells (lower). Scale bar, 50 μm. Data are presented as mean ± SEM from 150 cells across seven images obtained from three independent experiments. $^{**}P < .01$, $^{***}P < .001$, one-way ANOVA followed by Dunnett's multiple comparisons test. (**B**) GSEA plot showing enrichment of cellular senescence-related genes in RNA-seq data from *Nsmf*$^{+/+}$; *Apc*$^{Min/+}$ and *Nsmf*$^{-/-}$; *Apc*$^{Min/+}$ intestinal tumor (upper). Heatmap visualization of differentially expressed senescence- and SASP-related genes between genotypes (lower). (**C**) qRT-PCR analysis of senescence-associated genes in intestinal tumors from *Nsmf*$^{+/+}$; *Apc*$^{Min/+}$ ($n = 4$) and *Nsmf*$^{-/-}$; *Apc*$^{Min/+}$ ($n = 3$) mice. Data represent the mean ± SEM. $^{*}P < .05$, $^{**}P < .01$, $^{***}P < .001$, unpaired two-tailed *t*-test with Holm–Sidak correction for multiple comparisons. (**D**) Western blot analysis of p16INK4A and p21CIP1 in intestinal tumor tissues from *Nsmf*$^{+/+}$; *Apc*$^{Min/+}$ and *Nsmf*$^{-/-}$; *Apc*$^{Min/+}$ mice. GAPDH served as a loading control. (**E**) Schematic representation of the experimental design for the oncogene-induced senescence model. IMR-90 cells were transduced with lentiviruses encoding either GFP-vector or GFP-NSMF. Following selection, senescence was induced by expression of oncogenic Ras^{G12V}. (**F**) Western blot analysis of the indicated proteins on day 4 after induction of oncogenic Ras^{G12V} expression. α-Tubulin was used as a loading control. (**G**) SA-β-Gal staining in IMR-90 cells 8 days post-transduction. Representative images (left) and quantification of SA-β-Gal positive cells (right). Scale bar, 20um. Data are presented as mean ± SEM ($n = 4$–6 independent images per sample). $^{***}P <$ .001, n.s., not significant, one-way ANOVA followed by Tukey's HSD test. (**H**) Immunofluorescence analysis of γH2AX in GFP-vector or GFP-NSMF expressing IMR-90 cells with or without Ras^{G12V}. Quantification of γH2AX foci per GFP-positive cell was performed in at least 42 cells per group. Scale bar, 20 μm. Data are presented as median. $^{**}P < .01$, $^{****}P < .0001$, n.s., not significant, Kruskal–Wallis test followed by Dunn's multiple comparisons test. All experiments were independently performed at least three times, and representative results are shown. (**I**) Correlation of NSMF expression with genomic instability in pan-cancer analysis. Genomic instability was assessed across 4315 pan-cancer samples from TCGA using multiple genomic instability features, including frequency of LOH, HRD-related LOH frequency, telomeric allelic imbalance, large-scale transitions, mutation burden per sample, and weighted genome integrity index. Tumors were categorized based on genomic instability scores as low (<25%, below first quartile), medium (25%–75%, between first and third quartile), or high (>75%, above third quartile). Statistical comparisons of NSMF expression levels across groups were performed using Wilcoxon rank-sum test. (**J**) Hypothetical model illustrating the role of NSMF in regulating replication stress, highlighting its critical function in alleviating excessive replication stress and preventing cytotoxic DNA damage. This regulatory activity supports a controlled level of genomic instability, thereby promoting CRC progression. Figure was created using BioRender.com.

sues, NSMF and γH2AX were co-overexpressed, further supporting NSMF's role in replication stress regulation (Fig. 1J). Additionally, we observed a strong positive correlation between NSMF expression and replication stress scores in both tumor tissues and CRC cell lines (Figs 1C and 4A). Notably, while NSMF is dispensable for normal intestinal homeostasis, its loss in $Apc^{Min/+}$ mice significantly impaired adenoma formation and prolonged survival (Fig. 2 and Supplementary Fig. S2). The selective increase in replication stress and DNA damage observed in tumor tissues of NSMF-deficient mice, as evidenced by elevated γH2AX and transcriptional upregulation of DDR genes, suggests that NSMF plays a key role in managing high-replication stress conditions in tumor cells (Fig. 3). This also explains why NSMF deletion had no significant effect on normal intestinal homeostasis, where replication stress is inherently lower. Collectively, our findings establish NSMF as an essential factor for cancer cell survival and growth. Targeting NSMF could exacerbate replication stress in cancer cells beyond their adaptive capacity, thereby inhibiting tumor growth without significantly affecting normal tissues.

In this study, we employed a systematic and comprehensive approach to identify previously uncharacterized regulators of replication stress in cancer by employing a quantitative replication stress-assessment strategy. Because replication stress can originate from diverse sources and exhibit heterogeneous manifestations, its accurate measurement remains challenging. This complexity is further compounded by the diverse cellular context and heterogeneity of tumors. Although traditional markers such as ssDNA-bound RPA and γH2AX have been widely used in experimental models, their applicability in large-scale clinical settings and their ability to capture the full spectrum of replication stress regulators across various cancer contexts are limited. To address these challenges, several research groups have explored alternative methods for quantifying replication stress [40, 62, 63]. We adopted a model that integrates 21 distinct pathways, each representing different aspects of replication stress, to generate a comprehensive measure of replication stress levels [40]. Using this approach, we applied transcriptional profiling to identify gene expression signatures associated with DNA replication and repair and analyzed their correlation with replication stress in CRC. To identify key regulators of replication stress that contribute to tumor survival and growth, we prioritized genes that were overexpressed in tumors compared to normal tissues and that also correlated with patient prognosis. Furthermore, to focus on novel regulators rather than those already well-characterized, we excluded 844 genes that were part of the 21 GO pathway. Through this systematic approach, we identified 17 previously uncharacterized regulators of replication stress, including NSMF, which had not been implicated in replication stress regulation in the context of cancer (Fig. 1A and Supplementary Fig. S1A). Given that replication stress plays a critical role in the development of most cancer types, this strategy is broadly applicable and may enable the identification of replication stress regulators specific to various tumor types and their progression stages.

The RPA–ssDNA complex provides a crucial platform for recruiting various DNA repair proteins—such as ATR, ATRIP, and PRP19—to stalled replication forks, thereby coordinating the DDR signaling pathway and facilitating DNA repair [64]. Our previous studies have shown that NSMF directly interacts with RPA, stabilizing the RPA–ssDNA complex and promoting ATR-mediated phosphorylation of RPA under replication stress conditions [30]. Consequently, NSMF aids in replication fork stabilization and activates the ATR-CHK1 checkpoint pathway in response to replication stress. In NSMF-depleted cells, the compromised interaction between RPA and ssDNA results in a diminished repair response and an accumulation of DNA damage [31]. Consistent with this mechanism, NSMF knockdown led to reduced formation and phosphorylation of RPA foci, while γH2AX levels were elevated under replication stress (Fig. 5E and F). Furthermore, NSMF-depleted cells exhibited a slower decline in γH2AX levels during the recovery phase following HU treatment, along with delayed cell cycle progression (Fig. 5D). These data suggest that NSMF enhances DDR signaling, mitigates replication stress, and facilitates efficient recovery from replication stress, thereby preventing severe DNA damage. Interestingly, NSMF depletion causes cell cycle defects and promotes cellular senescence without an increase in apoptosis (Figs 4E, 6A and S6A–D). In both CRC cells and primary fibroblasts, loss of NSMF led to enhanced senescence. Similarly, in $Apc^{Min/+}$ mice, *Nsmf* depletion reduced cell proliferation in tumor regions while increasing senescence (Fig. 6B–D). This association between NSMF and cellular senescence was further demonstrated in an oncogene-induced senescence model. It is well established that oncogene activation, such as *RAS*, *RAF*, *MYC*, and *Cyclin E1*, triggers growth arrest and senescence due to replication stress-mediated DNA damage [54]. Overexpression of NSMF alleviated Ras^{G12V}-induced replication stress and senescence in IMR90 fibroblasts, suggesting that NSMF counteracts oncogene-induced senescence by mitigating replication stress and preventing the accumulation of excessive DNA damage (Fig. 6E–H). Overall, our findings indicate that NSMF acts as a critical factor that enables cancer cells to balance replication stress tolerance and evade senescence, rendering it indispensable for all stages of tumor development and growth.

In tumors with defects in homologous recombination repair (e.g. *BRCA1/2*-mutated cancers), combining replication stress inducers with PARP inhibitors can selectively kill cancer cells while sparing normal cells, and this approach is widely used in the clinic [65, 66]. However, beyond the success seen in BRCA-mutated cancers, synthetic lethal combinations have generally been less effective in clinical settings due to tumor heterogeneity and the presence of genetically diverse clones [67, 68]. In CRC, efforts to therapeutically target DDR and replication stress pathways—particularly through PARP, ATR, CHK1, and WEE1 inhibitors—are actively underway [69]. Preclinical and early-phase clinical trials have shown that ATR inhibitors, CHK1 inhibitors and WEE1 inhibitors can enhance the effects of chemotherapy in DDR-deficient CRC [70–72]. Moreover, PARP inhibitors appear promising in microsatellite stable, pMMR CRC, and their clinical efficacy is maximized when combined with DNA repair-related agents or DNA-damaging agents, rather than as monotherapy [69]. Nevertheless, the absence of robust predictive biomarkers for replication stress dependency and the limited response observed in unselected CRC patients remain major challenges for clinical translation [2, 69]. Identifying regulators that define replication stress tolerance is therefore essential for refining therapeutic stratification. Given its role in mitigating replication stress and promoting tumor growth, NSMF represents a potential therapeutic target in cancer. In our study, we demonstrated that NSMF depletion alone suppresses tu-

mor initiation and growth. Moreover, we found that NSMF expression is significantly elevated in most CRC patients and that high levels correlate with poor prognosis. Interestingly, NSMF knockdown in CRC cells also increased sensitivity to DDR pathway PARP1, ATR, and CHK1 kinase inhibitors. In contrast, NSMF loss did not alter sensitivity to conventional DNA-damaging chemotherapeutic agents such as cisplatin or doxorubicin. This divergence suggests that NSMF functions selectively in replication-coupled DNA repair and replication stress tolerance, rather than mediating resistance to general cytotoxic agents. The therapeutic potential of targeting NSMF lies in its ability to exploit tumor-specific dependency on replication stress resilience. Tumors with intrinsically high replication stress appear disproportionately reliant on NSMF for survival, making NSMF inhibition a strategy that could selectively induce replication collapse in tumor cells while minimizing toxicity in normal tissues. Furthermore, the widespread overexpression of NSMF across diverse malignancies highlights its broader relevance as a cancer vulnerability. Future studies should investigate NSMF's role in additional tumor types and evaluate NSMF as both a biomarker of replication stress dependency and a therapeutic target.

In conclusion, our study establishes NSMF as a pivotal regulator of replication stress in cancer, offering mechanistic insights into how tumor cells precisely balance replication stress to sustain proliferation and survival. By promoting replication fork progression and enhancing DDR signaling under stress conditions, NSMF enables cancer cells to maintain replication stress within a tumor-promoting threshold—enhancing genomic instability while avoiding catastrophic DNA damage—thereby facilitating tumor initiation and progression (Fig. 6J). Our study provides a conceptual framework highlighting replication stress modulation as a novel therapeutic strategy in CRC and potentially other malignancies characterized by elevated genomic instability.

Acknowledgements

We thank the staff members of the UNIST Central Research Facilities (UCRF) for technical support. Author Contributions: K.J.S. and Y.C.C. conceived the project. K.J.S. and Y.J.L. designed and conducted the majority of the experiments and analyzed the data. Y.J.L. and G.K. assisted with microscopic and mouse experiments. H.S.K. performed and analyzed data from mouse organoids. J.H.C. analyzed RNA sequencing data from patient samples. J.H.K., S.J.Y., K.L.K., S.P., J.H.C., D.H.P., H.W.K., S.C., K.L., and S.L. contributed to bioinformatics data analysis. K.M. and E.A.L. conducted the DNA fiber assay and analyzed the data. S.M.J. and M.S.J. collected and analyzed patient samples. K.J.S., Y.J.L., and Y.C.C. wrote the manuscript. All authors reviewed and approved the final version of the manuscript.

Author contributions: Yu Jin Lee (Conceptualization [equal], Writing—original draft [equal]), Gyuri Kim (Investigation [supporting]), Seongjun You (Investigation [supporting]), Kyung Lock Kim (Formal analysis [supporting]), Sabin Park (Formal analysis [supporting]), KyoungJun Lee (Formal analysis [supporting]), Do Hong Park (Formal analysis [supporting]), Hui Won Kim (Formal analysis [supporting]), Sanga Choi (Formal analysis [supporting]), Sung Min Jung (Methodology [supporting]), Jung-Hyun Kim (Investigation [supporting]), Hyung-Sik Kim (Methodology [supporting]), and Seung-Jae Myung (Investigation [supporting])

Supplementary data

Supplementary data is available at NAR online.

Conflict of interest

None declared.

Funding

This work was supported by grants from the National Research Foundation of Korea funded by the Ministry of Education (2018R1A6A1A03025810, 2022R1I1A1A01068234, and 2022R1I1A4053049), the Ministry of Science and ICT (RS-2023-00211744, 2023R1A2C2005342, and RS-2025-20552973), and the Ministry of Trade, Industry and Energy (RS-2024-00403190). Funding to pay the Open Access publication charges for this article was provided by the National Research Foundation of Korea, funded by the Ministry of Trade, Industry and Energy RS-2024-00403190.

Data availability

RNA sequencing data from human colorectal cancer patients and mouse colon tumors generated in this study have been deposited in the National Center for Biotechnology Information Gene Expression Omnibus (GEO) under accession code GSE298852. Additional information required to reanalyze the data reported in this paper, as well as plasmids and cell lines generated in this work, is available from the lead contact upon reasonable request.

References

1. Fragkos M, Ganier O, Coulombe P *et al.* DNA replication origin activation in space and time. *Nat Rev Mol Cell Biol* 2015;16:360–74. https://doi.org/10.1038/nrm4002
2. da Costa A, Chowdhury D, Shapiro GI *et al.* Targeting replication stress in cancer therapy. *Nat Rev Drug Discov* 2023;22:38–58. https://doi.org/10.1038/s41573-022-00558-5
3. Hamperl S, Bocek MJ, Saldivar JC *et al.* Transcription–replication conflict orientation modulates R-loop levels and activates distinct DNA damage responses. *Cell* 2017;170:774–786.e19. https://doi.org/10.1016/j.cell.2017.07.043
4. Donne R, Saroul-Ainama M, Cordier P *et al.* Replication stress triggered by nucleotide pool imbalance drives DNA damage and cGAS-STING pathway activation in NAFLD. *Dev Cell* 2022;57:1728–1741.e6. https://doi.org/10.1016/j.devcel.2022.06.003
5. Bohly N, Schmidt AK, Zhang X *et al.* Increased replication origin firing links replication stress to whole chromosomal instability in human cancer. *Cell Rep* 2022;41:111836. https://doi.org/10.1016/j.celrep.2022.111836
6. Williams SL, Casas-Delucchi CS, Raguseo F *et al.* Replication-induced DNA secondary structures drive fork uncoupling and breakage. *EMBO J* 2023;42:e114334. https://doi.org/10.15252/embj.2023114334
7. Menolfi D, Lee BJ, Zhang H *et al.* ATR kinase supports normal proliferation in the early S phase by preventing replication resource exhaustion. *Nat Commun* 2023;14:3618. https://doi.org/10.1038/s41467-023-39332-5
8. Igarashi T, Mazevet M, Yasuhara T *et al.* An ATR-PrimPol pathway confers tolerance to oncogenic KRAS-induced and heterochromatin-associated replication stress. *Nat Commun* 2023;14:4991. https://doi.org/10.1038/s41467-023-40578-2

9. Saxena S, Zou L. Hallmarks of DNA replication stress. *Mol Cell* 2022;82:2298–314. https://doi.org/10.1016/j.molcel.2022.05.004
10. Cybulla E, Vindigni A. Leveraging the replication stress response to optimize cancer therapy. *Nat Rev Cancer* 2023;23:6–24. https://doi.org/10.1038/s41568-022-00518-6
11. Bakhoum SF, Cantley LC. The multifaceted role of chromosomal instability in cancer and its microenvironment. *Cell* 2018;174:1347–60. https://doi.org/10.1016/j.cell.2018.08.027
12. Negrini S, Gorgoulis VG, Halazonetis TD. Genomic instability–an evolving hallmark of cancer. *Nat Rev Mol Cell Biol* 2010;11:220–8. https://doi.org/10.1038/nrm2858
13. Dwivedi D, Harry D, Meraldi P. Mild replication stress causes premature centriole disengagement via a sub-critical Plk1 activity under the control of ATR-Chk1. *Nat Commun* 2023;14:6088. https://doi.org/10.1038/s41467-023-41753-1
14. Reilly NM, Novara L, Di Nicolantonio F *et al.* Exploiting DNA repair defects in colorectal cancer. *Mol Oncol* 2019;13:681–700. https://doi.org/10.1002/1878-0261.12467
15. Nguyen DD, Kim E, Le NT *et al.* Deficiency in mammalian STN1 promotes colon cancer development via inhibiting DNA repair. *Sci Adv* 2023;9:eadd8023. https://doi.org/10.1126/sciadv.add8023
16. Durinikova E, Reilly NM, Buzo K *et al.* Targeting the DNA damage response pathways and replication stress in colorectal cancer. *Clin Cancer Res* 2022;28:3874–89. https://doi.org/10.1158/1078-0432.CCR-22-0875
17. Lee S, Schmitt CA. The dynamic nature of senescence in cancer. *Nat Cell Biol* 2019;21:94–101. https://doi.org/10.1038/s41556-018-0249-2
18. Collado M, Gil J, Efeyan A *et al.* Tumour biology: senescence in premalignant tumours. *Nature* 2005;436:642. https://doi.org/10.1038/436642a
19. Bartkova J, Rezaei N, Liontos M *et al.* Oncogene-induced senescence is part of the tumorigenesis barrier imposed by DNA damage checkpoints. *Nature* 2006;444:633–7. https://doi.org/10.1038/nature05268
20. Ngoi NYL, Pham MM, Tan DSP *et al.* Targeting the replication stress response through synthetic lethal strategies in cancer medicine. *Trends Cancer* 2021;7:930–57. https://doi.org/10.1016/j.trecan.2021.06.002
21. Parmar K, Kochupurakkal BS, Lazaro JB *et al.* The CHK1 inhibitor prexasertib exhibits monotherapy activity in high-grade serous ovarian cancer models and sensitizes to PARP inhibition. *Clin Cancer Res* 2019;25:6127–40. https://doi.org/10.1158/1078-0432.CCR-19-0448
22. Sen T, Tong P, Stewart CA *et al.* CHK1 Inhibition in small-cell lung cancer produces single-agent activity in biomarker-defined disease subsets and combination activity with cisplatin or olaparib. *Cancer Res* 2017;77:3870–84. https://doi.org/10.1158/0008-5472.CAN-16-3409
23. Bukhari AB, Lewis CW, Pearce JJ *et al.* Inhibiting Wee1 and ATR kinases produces tumor-selective synthetic lethality and suppresses metastasis. *J Clin Invest* 2019;129:1329–44. https://doi.org/10.1172/JCI122622
24. Li Q, Qian W, Zhang Y *et al.* A new wave of innovations within the DNA damage response. *Sig Transduct Target Ther* 2023;8:338. https://doi.org/10.1038/s41392-023-01548-8
25. Yap TA, Fontana E, Lee EK *et al.* Camonsertib in DNA damage response-deficient advanced solid tumors: phase 1 trial results. *Nat Med* 2023;29:1400–11. https://doi.org/10.1038/s41591-023-02399-0
26. Hardaker EL, Sanseviero E, Karmokar A *et al.* The ATR inhibitor ceralasertib potentiates cancer checkpoint immunotherapy by regulating the tumor microenvironment. *Nat Commun* 2024;15:1700. https://doi.org/10.1038/s41467-024-45996-4
27. Miura K, Acierno JS, Seminara SB. Characterization of the human nasal embryonic LHRH factor gene, NELF, and a mutation screening among 65 patients with idiopathic hypogonadotropic hypogonadism (IHH). *J Hum Genet* 2004;49:265–8. https://doi.org/10.1007/s10038-004-0137-4
28. Pitteloud N, Quinton R, Pearce S *et al.* Digenic mutations account for variable phenotypes in idiopathic hypogonadotropic hypogonadism. *J Clin Invest* 2007;117:457–63. https://doi.org/10.1172/JCI29884
29. Kramer PR, Wray S. Novel gene expressed in nasal region influences outgrowth of olfactory axons and migration of luteinizing hormone-releasing hormone (LHRH) neurons. *Genes Dev* 2000;14:1824–34. https://doi.org/10.1101/gad.14.14.1824
30. Ju MK, Shin KJ, Lee JR *et al.* NSMF promotes the replication stress-induced DNA damage response for genome maintenance. *Nucleic Acids Res* 2021;49:5605–22. https://doi.org/10.1093/nar/gkab311
31. Kang Y, Han YG, Khim KW *et al.* Alteration of replication protein A binding mode on single-stranded DNA by NSMF potentiates RPA phosphorylation by ATR kinase. *Nucleic Acids Res* 2023;51:7936–50. https://doi.org/10.1093/nar/gkad543
32. Park SH, Kang N, Song E *et al.* ATAD5 promotes replication restart by regulating RAD51 and PCNA in response to replication stress. *Nat Commun* 2019;10:5718. https://doi.org/10.1038/s41467-019-13667-4
33. Klemke L, Blume JP, De Oliveira T *et al.* Preparation and cultivation of colonic and small intestinal murine organoids including analysis of gene expression and organoid viability. *Bio Protoc* 2022;12:e4298. https://doi.org/10.21769/BioProtoc.4298
34. Bolger AM, Lohse M, Usadel B. Trimmomatic: a flexible trimmer for illumina sequence data. *Bioinformatics* 2014;30:2114–20. https://doi.org/10.1093/bioinformatics/btu170
35. Dobin A, Davis CA, Schlesinger F *et al.* STAR: ultrafast universal RNA-seq aligner. *Bioinformatics* 2013;29:15–21. https://doi.org/10.1093/bioinformatics/bts635
36. Li B, Dewey CN. RSEM: accurate transcript quantification from RNA-Seq data with or without a reference genome. *BMC Bioinformatics* 2011;12:323. https://doi.org/10.1186/1471-2105-12-323
37. Love MI, Huber W, Anders S. Moderated estimation of fold change and dispersion for RNA-seq data with DESeq2. *Genome Biol* 2014;15:550. https://doi.org/10.1186/s13059-014-0550-8
38. Subramanian A Tamayo P, Mootha VK *et al.*, Gene set enrichment analysis: a knowledge-based approach for interpreting genome-wide expression profiles. *Proc Natl Acad Sci U S A* 2005;102:15545–50.https://doi.org/10.1073/pnas.0506580102
39. Mootha VK Lindgren CM, Eriksson KF *et al.*, PGC-1alpha-responsive genes involved in oxidative phosphorylation are coordinately downregulated in human diabetes. *Nat Genet* 2003;34:267–73.https://doi.org/10.1038/ng1180
40. Dreyer SB, Upstill-Goddard R, Paulus-Hock V *et al.* Targeting DNA damage response and replication stress in pancreatic cancer. *Gastroenterology* 2021;160:362–77.e13. https://doi.org/10.1053/j.gastro.2020.09.043
41. Marquard AM, Eklund AC, Joshi T *et al.* Pan-cancer analysis of genomic scar signatures associated with homologous recombination deficiency suggests novel indications for existing cancer drugs. *Biomark Res* 2015;3:9. https://doi.org/10.1186/s40364-015-0033-4
42. Kim W, Zhao F, Wu R *et al.* ZFP161 regulates replication fork stability and maintenance of genomic stability by recruiting the ATR/ATRIP complex. *Nat Commun* 2019;10:5304. https://doi.org/10.1038/s41467-019-13321-z
43. McGrail DJ, Lin CC-J, Dai H *et al.* Defective replication stress response is inherently linked to the cancer stem cell phenotype. *Cell Rep* 2018;23:2095–106. https://doi.org/10.1016/j.celrep.2018.04.068
44. Guerrero Llobet S, Bhattacharya A, Everts M *et al.* An mRNA expression-based signature for oncogene-induced replication-stress. *Oncogene* 2022;41:1216–24. https://doi.org/10.1038/s41388-021-02162-0
45. Paul MC, Schneeweis C, Falcomatà C *et al.* Non-canonical functions of SNAIL drive context-specific cancer progression. *Nat*

Commun 2023;14:1201. https://doi.org/10.1038/s41467-023-36505-0
46. Huang W, Han Z, Sun Z *et al.* PAK6 promotes homologous-recombination to enhance chemoresistance to oxaliplatin through ATR/CHK1 signaling in gastric cancer. *Cell Death Dis* 2022;13:658. https://doi.org/10.1038/s41419-022-05118-8
47. Wu Q, Zheng Q, Yuan L *et al.* Repression of YEATS2 induces cellular senescence in hepatocellular carcinoma and inhibits tumor growth. *Cell Cycle* 2024;23:478–94. https://doi.org/10.1080/15384101.2024.2342714
48. Zhang L, Li DQ. MORC2 regulates DNA damage response through a PARP1-dependent pathway. *Nucleic Acids Res* 2019;47:8502–20. https://doi.org/10.1093/nar/gkz545
49. Spilker C, Nullmeier S, Grochowska KM *et al.* A Jacob/Nsmf gene knockout results in hippocampal dysplasia and impaired BDNF signaling in dendritogenesis. *PLoS Genet* 2016;12:e1005907. https://doi.org/10.1371/journal.pgen.1005907
50. Oshima M, Oshima H, Kitagawa K *et al.* Loss of Apc heterozygosity and abnormal tissue building in nascent intestinal polyps in mice carrying a truncated Apc gene. *Proc Natl Acad Sci USA* 1995;92:4482–6. https://doi.org/10.1073/pnas.92.10.4482
51. Chun SK, Fortin BM, Fellows RC *et al.* Disruption of the circadian clock drives Apcloss of heterozygosity to accelerate colorectal cancer. *Sci Adv* 2022;8:eabo2389. https://doi.org/10.1126/sciadv.abo2389
52. Kotsantis P, Petermann E, Boulton SJ. Mechanisms of oncogene-induced replication stress: jigsaw falling into place. *Cancer Discov* 2018;8:537–55. https://doi.org/10.1158/2159-8290.CD-17-1461
53. Di Micco R, Fumagalli M, Cicalese A *et al.* Oncogene-induced senescence is a DNA damage response triggered by DNA hyper-replication. *Nature* 2006;444:638–42. https://doi.org/10.1038/nature05327
54. Villot R, Poirier A, Bakan I *et al.* ZNF768 links oncogenic RAS to cellular senescence. *Nat Commun* 2021;12:4841. https://doi.org/10.1038/s41467-021-24932-w
55. Aird KM, Zhang G, Li H *et al.* Suppression of nucleotide metabolism underlies the establishment and maintenance of oncogene-induced senescence. *Cell Rep* 2013;3:1252–65. https://doi.org/10.1016/j.celrep.2013.03.004
56. Tomasetti C, Li L, Vogelstein B. Stem cell divisions, somatic mutations, cancer etiology, and cancer prevention. *Science* 2017;355:1330–4. https://doi.org/10.1126/science.aaf9011
57. Zhang T, Künne C, Ding D *et al.* Replication collisions induced by de-repressed S-phase transcription are connected with malignant transformation of adult stem cells. *Nat Commun* 2022;13:6907. https://doi.org/10.1038/s41467-022-34577-y
58. Hosea R, Hillary S, Naqvi S *et al.* The two sides of chromosomal instability: drivers and brakes in cancer. *Sig Transduct Target Ther* 2024;9:75. https://doi.org/10.1038/s41392-024-01767-7
59. Peripolli S, Meneguello L, Perrod C *et al.* Oncogenic c-Myc induces replication stress by increasing cohesins chromatin occupancy in a CTCF-dependent manner. *Nat Commun* 2024;15:1579. https://doi.org/10.1038/s41467-024-45955-z
60. Macheret M, Halazonetis TD. Intragenic origins due to short G1 phases underlie oncogene-induced DNA replication stress. *Nature* 2018;555:112–6. https://doi.org/10.1038/nature25507
61. Kotsantis P, Silva LM, Irmscher S *et al.* Increased global transcription activity as a mechanism of replication stress in cancer. *Nat Commun* 2016;7:13087. https://doi.org/10.1038/ncomms13087
62. Takahashi N, Kim S, Schultz CW *et al.* Replication stress defines distinct molecular subtypes across cancers. *Cancer Research Communications* 2022;2:503–17. https://doi.org/10.1158/2767-9764.CRC-22-0168
63. Huang R-H, Hong Y-K, Du H *et al.* A machine learning framework develops a DNA replication stress model for predicting clinical outcomes and therapeutic vulnerability in primary prostate cancer. *J Transl Med* 2023;21:20. https://doi.org/10.1186/s12967-023-03872-7
64. Maréchal A, Zou L. RPA-coated single-stranded DNA as a platform for post-translational modifications in the DNA damage response. *Cell Res* 2015;25:9–23. https://doi.org/10.1038/cr.2014.147
65. Bryant HE, Schultz N, Thomas HD *et al.* Specific killing of BRCA2-deficient tumours with inhibitors of poly(ADP-ribose) polymerase. *Nature* 2005;434:913–7. https://doi.org/10.1038/nature03443
66. Farmer H, McCabe N, Lord CJ *et al.* Targeting the DNA repair defect in BRCA mutant cells as a therapeutic strategy. *Nature* 2005;434:917–21. https://doi.org/10.1038/nature03445
67. Topatana W, Juengpanich S, Li S *et al.* Advances in synthetic lethality for cancer therapy: cellular mechanism and clinical translation. *J Hematol Oncol* 2020;13:118. https://doi.org/10.1186/s13045-020-00956-5
68. Drew Y, Zenke FT, Curtin NJ. DNA damage response inhibitors in cancer therapy: lessons from the past, current status and future implications. *Nat Rev Drug Discov* 2025;24:19–39. https://doi.org/10.1038/s41573-024-01060-w
69. Alese OB, Wu C, Chapin WJ *et al.* Update on emerging therapies for advanced colorectal cancer. *Am Soc Clin Oncol Educ Book* 2023;43 e389574. https://doi.org/10.1200/EDBK_389574
70. Yap TA, O'Carrigan B, Penney MS *et al.* Phase I trial of first-in-class ATR inhibitor M6620 (VX-970) as monotherapy or in combination with carboplatin in patients with advanced solid tumors. *J Clin Oncol* 2020;38:3195–204. https://doi.org/10.1200/JCO.19.02404
71. Inoue A, Robinson FS, Minelli R *et al.* Sequential administration of XPO1 and ATR inhibitors enhances therapeutic response in TP53-mutated colorectal cancer. *Gastroenterology* 2021;161:196–210. https://doi.org/10.1053/j.gastro.2021.03.022
72. Seligmann JF, Fisher DJ, Brown LC *et al.* Inhibition of WEE1 is effective in TP53- and RAS-mutant metastatic colorectal cancer: a randomized trial (FOCUS4-C) comparing adavosertib (AZD1775) with active monitoring. *JCO* 2021;39:3705–15. https://doi.org/10.1200/JCO.21.01435

Received: August 12, 2025. **Revised:** November 30, 2025. **Accepted:** December 20, 2025